

Abstract

This thesis is motivated by the need for noise control in aircraft engine with orifices and perforated liner. The presence of high-level acoustic excitation, different flow situations either bias flow, grazing flow or any combination in the aircraft engine, makes the acoustic behavior complex due to the interaction between sound and flow over the lined wall. Both systematic acoustic prediction of aircraft engines and liner optimization necessitate progress in impedance measurement methods by including the effect of the complex flow situations. The aim of the present thesis is to experimentally study the change in acoustic properties of orifices and perforated liners under bias or grazing flow.

In order to study the effect of different combinations of bias flow and high-level acoustic excitation, an in-duct orifice has been investigated with finely controlled acoustic excitation levels and bias flow speeds. This provides a detailed study of the transition from cases when high-level acoustic excitation causes flow reversal in the orifice to cases when the bias flow maintains the flow direction. Nonlinear impedance is measured and compared, and a scattering matrix and its eigenvalues are investigated to study the potentiality of acoustic energy dissipation or production. A harmonic method is proposed for modelling the impedance, especially the resistance, which captures the change in impedance results at low frequencies compared with experimental results.

The presence of grazing flow can increase the resistance of acoustic liners and shift their resonator frequency. So-called impedance eduction technology has been widely studied during the past decades, but with a limited confidence due to the interaction of grazing flow and acoustic waves. A comparison has been performed with different test rigs and methods from the German Aerospace Center (DLR). Numerical work has been performed to investigate the effect of shear flow and viscosity. Our study indicates that the impedance eduction process should be consistent with that of the code of wave propagation computation, for example with the same assumption regarding shear flow and viscosity. A systematic analysis for measurement uncertainties is proposed in order to understand the essentials for data quality assessment and model validation. The idea of using different Mach numbers for wave dispersion and in the Ingard-Myers boundary condition has been tested regarding their effect on impedance eduction. In conclusion, a local Mach number based on friction velocity is introduced and validated using both our own experimental results and those of previous studies.

Keywords: Bias Flow, Grazing Flow, Nonlinear Acoustics, Acoustic Impedance, Impedance Eduction, Single Mode Straightforward Method, Uncertainty Analysis, LEE, LNSE.

Sammanfattning

Detta arbete motiveras av behovet av bullerbekämpning för flygplansmotorer. Den vanligaste typen av bullerdämpande väggbeklädnad använder perforerade ytor kombinerade med kaviteter, s.k. akustiska liners. De akustiska egenskaperna för dessa perforerade ytor är komplexa på grund av inverkan av medelströmning, både strykande och genom perforeringarna, samt höga akustiska excitationnivåer. Prediktering av ljud från flygplansmotorer och optimering av akustiska liners kräver fortsatt utveckling av metoder för mätning av akustisk impedans för liners. Speciellt för att inkludera effekter av strömning och akustisk excitering med höga nivåer. Syftet med denna studie är att experimentellt undersöka påverkan på akustiska egenskaper hos liners av strömning och akustisk excitering, samt att utveckla förbättrade experimentella metoder för denna typ av mätningar.

För att studera effekten av olika kombinationer av strömning genom perforeringar och akustisk excitering med höga nivåer, har strypningar monterade i en kanal använts. Detta har gett möjlighet att systematiskt variera strömningshastigheten och nivån på den akustiska exciteringen så att en detaljerad studie av övergången från fall där den akustiska exciteringen orsakar en återströmning genom strypningen till fall där strömningen genom strypningen dominerar. Mätning av s.k. icke-linjär impedans har utförts. En spridningsmatris och dess egenvärden har studerats och använts för att bedömma potentialen för generering eller dissipation av akustisk energi. En metod som använder harmonisk balans har utvecklats för att modellera impedansen, speciellt resistansen, och jämförelser med de experimentella resultaten har gjorts.

Strykande medelströmning kan öka resistansen hos akustiska liners och ändra dess resonansfrekvens. Inversa metoder för experimentell bestämning av akustisk impedans har studerats flitig under de senaste decennierna, men effekterna av realistisk medelströmning kräver fortfarande ytterligare studier. En jämförande studie har genomförts där samma akustiska liner har testats i olika testriggar på KTH och det Tyska flygforskningsinstitutet DLR. Numerisk simulering har använts för att studera effekten av skjuvad strömning och viskositet. Resultaten visar att samma antaganden när det gäller strömningsprofil och effekten av viskositet bör användas både för bestämning av impedansen och när den används som randvillkor i ett beräkningsprogram. En systematisk analysmetod för studium av mätosäkerhet har utvecklats vilket är väsentligt för att skatta mätningarnas kvalitet. En ny tillämpning av Ingard-Myers randvillkor har utvecklats där ett lokalt Mach-tal föreslås för att förbättra impedansbestämningen. Resultat där detta nya randvillkor används har validerats både med användning av mätningar på KTH och resultat från litteraturen.

Nyckelord: Genomströmning, strykande medelströmning, icke-linjär akustik, akustisk impedans, inversa metoder för impedansmätning, osäkerhetsanalys, LEE, LNSE.

Acknowledgements

This research is financially supported by the KTH-CSC programme, which is a cooperation between KTH and the China Scholarship Council (CSC). Experimental work has been conducted in CCGEx (the Competence Centre for Gas Exchange) and MWL (the Marcus Wallenberg Laboratory for Sound and Vibration Research). Travel grants, Erik Petersohns Minne and the Signeul Fund are greatly acknowledged.

First of all, I would like to thank my main supervisor, Prof. Hans Bodén, for formulating the research problem at the beginning, helping and discussing any kind of research-related topic. It has been a pleasure to work together and I am looking forward to any cooperation in the future. I would like to thank my second supervisor, Prof. Mats Åbom, who invited me to Sweden, helped me with the application for the KTH-CSC programme and discussed the research work.

I really appreciate the friendly working atmosphere of the Department of Aeronautical and Vehicle Engineering. It has been my pleasure to meet so many wonderful people who have been or still are working in MWL and the department. I would like to thank Heiki, Luck and Raimo for their help and discussions during my experimental work. Dr. Nils Tillmark is acknowledged for his support in the CCGEx lab. I would like to thank Dr. Claus Lahiri and Dr. Stefan Busse-Gerstengarbe in the German Aerospace Center (DLR) for providing the acoustic liner, results and comments. Our skillful laboratory engineer, Danilo Prelevic, deserves special thanks for the measurement preparation. I extend a heartfelt thank you to PhDs, seniors at the department and the CCGEx centre for discussions and talks during seminars, meetings, the nice fika and lunches. To my friends in the Lappis corridor and in Stockholm, I would say thank you for the happy moments with you.

Finally, to my family and my lovely wife, for your support, thank you.

Papers and manuscripts included in the doctoral thesis

- A. Lin Zhou, Hans Bodén, *Experimental investigation of an in-duct orifice with bias flow under medium and high level acoustic excitation*, International Journal of Spray and Combustion Dynamics, 6(3), 2014, 267-292.

Bodén formulated the problem and supervised the acoustic experiments. The acoustic experiments were conducted and analysed by Zhou.

- B. Lin Zhou, Hans Bodén, *The effect of combined high level acoustic excitation and bias flow on the acoustic properties of an in-duct orifice*, AIAA2013-2128, 19th AIAA/CEAS Aeroacoustics Conference May 27-29, 2013, Berlin, Germany.

Zhou developed the harmonic balance method for modelling and carried out the analysis with experimental results. The paper was written by Zhou under supervision of Bodén.

- C. Lin Zhou, Hans Bodén, Claus Lahiri, Friedrich Bake, Lars Enghardt, Stefan Busse-Gerstengarbe, and Tamer Elnady, *Comparison of impedance eduction results using different methods and test rigs*, AIAA 2014-2955, 20th AIAA/CEAS Aeroacoustics Conference, 16-20 June 2014, Atlanta, USA.

Bodén formulated the problem and supervised the acoustic liner experiments at KTH. Busse-Gerstengarbe provided the test results from DLR. The Matlab code for multi-mode method was written by Elnady and modified by Zhou. The paper was written by Zhou under the supervision of Bodén in discussion with Lahiri, Bake, Enghardt, Busse-Gerstengarbe, and Elnady.

- D. Lin Zhou, Hans Bodén, *Effect of viscosity on impedance eduction and validation*, submitted to AIAA journal.

Zhou developed the methodologies and carried out the numerical modeling. The paper was written by Zhou under supervision of Bodén.

- E. Lin Zhou, Hans Bodén, *A systematic uncertainty analysis for liner impedance eduction technology*, submitted to Journal of Sound and Vibration.

Zhou developed the methodologies and carried out the analysis. The paper was written by Zhou under supervision of Bodén.

The content of the thesis has been presented at the following conferences

The 10th international conference on Flow-induced Vibration & Flow-induced Noise (Fiv2012), Dublin, Ireland, 2012.

International Workshop in Sound and Vibration Research, Cairo Egypt, 2012.

19th AIAA/CEAS Aeroacoustics Conference (34th AIAA Aeroacoustics Conference), Berlin, Germany, 2013.

Intl Summer School and Workshop on Non-Normal and Nonlinear Effects in Aero- and Thermoacoustics, TU München 2013.

20th AIAA/CEAS Aeroacoustics Conference (35th AIAA Aeroacoustics Conference), Atlanta, Geogia, USA, 2014.

Contents

Abstract	i
Sammanfattning	ii
Acknowledgements	iii
I Overview and Summary	1
1 Introduction	3
2 Theory for wave propagation in flow ducts	8
2.1 Fundamental equations of fluid dynamics	8
2.2 Wave propagation in ducts	9
2.2.1 Modal decomposition for waves in circular and rectangular ducts	9
2.2.2 Losses at the walls	13
2.2.3 Linearized Navier-Stokes Equations (LNSE)	14
3 Experimental techniques for duct aeroacoustics	16
3.1 Measurement techniques for determining impedance	16
3.2 Scattering matrix identification based on two-port theory	19
4 Characteristics of an in-duct orifice with bias flow under high-level acoustic excitation	21
4.1 Impedance model	21
4.2 Nonlinear acoustic properties of an in-duct orifice with bias flow	23
4.2.1 The effect of combined high-level acoustic excitation and bias flow . . .	23
4.2.2 Nonlinear scattering matrix and energy dissipation/generation	26
4.3 Experimental setup	28
4.4 Some results and discussion	29
4.4.1 Impedance results	29
4.4.2 Energy dissipation/generation	32
5 Impedance eduction technique for acoustic liner with grazing flow	34
5.1 Grazing flow facility for impedance eduction	34
5.2 Strategy and methods	36
5.2.1 Single-mode straightforward method	38
5.2.2 Numerical methods	39
5.2.3 The DLR's Method	40

5.3	Impedance results and uncertainty estimation	41
5.3.1	Comparison of results from different test rigs	41
5.3.2	Numerical study with the linearized Navier-Stokes equations	42
5.3.3	Uncertainty analysis based on the single-mode straightforward method	45
5.3.4	Discussion on Mach number used in the Ingard-Myers boundary condition	48
6	Concluding remarks and future work	50
6.1	Concluding remarks	50
6.2	Future work	51
6.2.1	Impedance eduction technique under higher mode excitation	51
6.2.2	Permeability and flow instability for perforated liner	51
6.2.3	Numerical method development for the interaction of waves and turbulent flow	51
7	Summary of Appended Papers	53
	References	60
II	Appended Papers	61

Part I

Overview and Summary

Chapter 1

Introduction

Noise is a threat to health and well-being, and has even been called a modern plague [1]. A recent study shows that about 7.9 million adults in Europe suffer from sleep disturbance due to night-time noise from road traffic, rail traffic, air traffic or industrial activity [2]. Many noise sources are different kinds of engines, such as the internal combustion engines for vehicles or gas turbines for aircraft. The part of the engine noise that comes from the gas exchange system, both the intake and exhaust system, is considered in this thesis. Stricter noise regulation is being implemented by international noise regulatory authorities and governments, which has positioned acoustics as a key element in the development of novel engines. For aircraft engines, novel high bypass ratio design has dramatically decreased the engine jet noise, while making the fan noise one of the major noise sources [3].

To understand the work and noise radiation of a high by-pass ratio turbofan engine, see Fig. 1.1, air is first sucked into the inlet duct by the front fan, then split into two paths: the by-pass and the core duct. The by-pass duct is where most of the air flow passes through

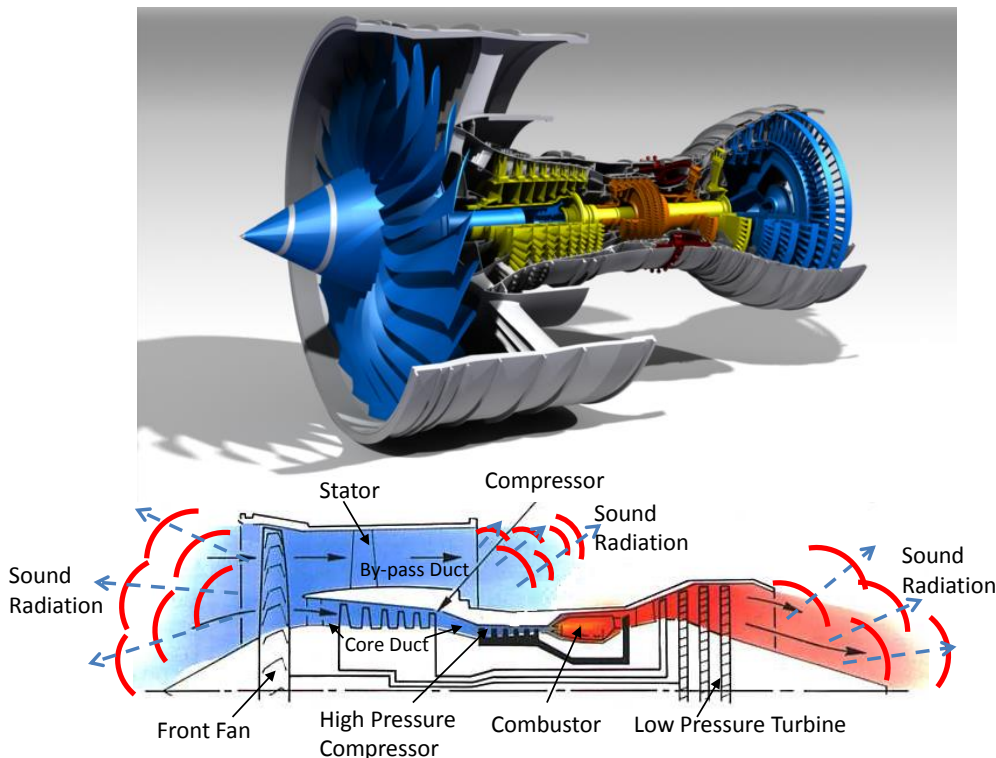


Figure 1.1: Sketch of a high by-pass turbofan engine and its sound radiation.

with a low flow speed. In the core duct, the air is compressed, mixed and burned with fuel in the combustor, and then pushed into the low-pressure turbine and exhausted. Different kinds of noise are produced in the process: fan noise, interaction noise produced by the the flow interaction between the front fan and the stator, combustion noise, turbine noise and jet noise produced by the exhaust flow. Before radiating to the outside aircraft engine, fan and core noise will have to propagate through either the by-pass or the core duct, which makes it possible to modify the wall treatment for noise attenuation. Fig. 1.2 shows some typical acoustic liners installed in an aero engine for sound attenuation. The basic liner model is

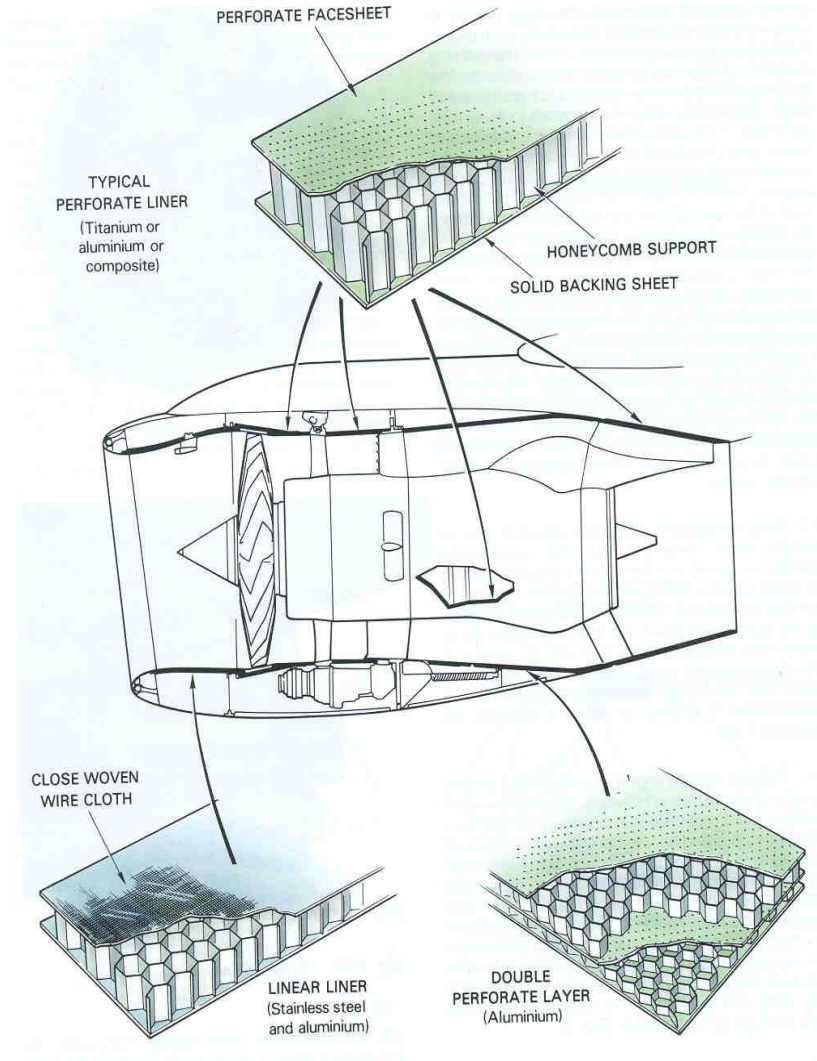


Figure 1.2: Typical perforate liner structures in turbine engine for sound attenuation [3].

called the single-degree-of-freedom liner (SDOF), consisting of a perforated plate covering a honeycomb structure and a solid back-plate. This type of liner performs like an array of single dimensional mass-spring damping systems. The air in the orifice plays the role of mass, and the cavity formed by the honeycomb structure acts as a spring. The acoustic energy dissipates because of friction losses when the air in the orifices is pumped back and forth. However, the liner can be exposed to high sound level excitation, bias flow, grazing flow, or any combination of these. These severe conditions mean that the properties of acoustic liners vary greatly and are difficult to predict. Indeed, wave propagation in aero engines with perforated liners is a multi-scale problem, because the wavelength is of metre scale

while the orifice is of or under millimetre scale. In addition, there is complex turbulent flow which means that a full model simulation including detailed flow in the small orifices is not feasible in the near future even with the fast developing computational capabilities. A more reasonable solution is to treat the liner as a boundary condition, for example by using the impedance $Z = \hat{p}/\hat{v}$ in the frequency domain, which is defined as ratio between the acoustic pressure \hat{p} and the inward normal component of the acoustic particle oscillating velocity \hat{v} [4]. The real part of impedance is called resistance and is related to energy dissipation while the imaginary part is called reactance and is related to kinetic energy stored or oscillating mass.

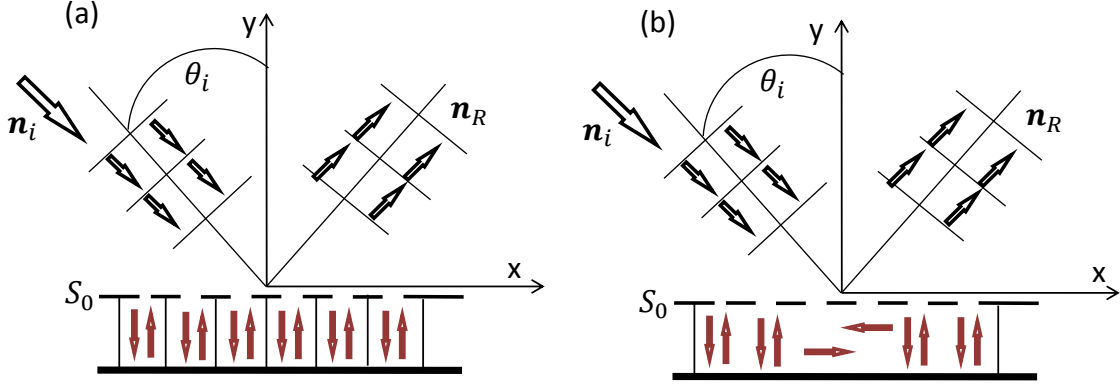


Figure 1.3: Reflection of plane wave with angle of incidence θ_i at surfaces over a locally reacting liner (a) and a non-locally reacting liner (b).

The liner surface could be modelled as locally reacting or non-locally reacting depending on whether the impedance is independent of the angle of incidence or not. Fig. 1.3 illustrates the reflection of a plane wave with angle of incidence θ_i at surface S_0 over a locally reacting liner and a non-locally reacting liner. The narrow chamber separation in the locally reacting liner confines wave propagation in each cell, which results in the value of normal velocity at a given point on the surface S_0 depend only on the acoustic pressure \hat{p} at the same point. This means that the impedance $Z = \hat{p}/\hat{v}$ is a scalar product and independent of the angle of incidence. On the other hand, for the non-locally liners in Fig. 1.3 with a large unseparated chamber, the pressure field over the surface S_0 can communicate through wave propagation in the chamber, which violates the local property of the acoustic field over the surface. Surfaces of most commercial lines can be idealized to be locally reacting. Examples are surfaces of Helmholtz resonator liners as shown in Fig. 1.2. The present study covers only reacting liners.

For low-level acoustic excitation, the acoustic impedance of perforated panels is linear and well-studied [5]. However, the acoustic properties can be dramatically modified by the acoustic-induced flow or the mean flow near or around the orifices in the case of high acoustic excitation levels and different mean flow structures. In most cases, the acoustic impedance is identified experimentally and implemented into wave propagation codes for turbo engine noise prediction. Obviously, the simulation and optimization are critically reliant on impedance measurement results. However, the identification process is not always straightforward, especially for high acoustic excitation levels under complex turbulent flow situations.

The present thesis focuses on the experimental technology development for orifice or acoustic liner impedance identification under different flows, either bias or grazing flow. This work began with an experimental investigation of an in-duct orifice. It is well known that

the acoustic properties of orifices play a key role in the performance of perforated liner structures. Since Sivian experimentally investigated the impedance of small orifices [6] and Rayleigh initialized the theory for acoustic behaviour of small cavity-backed resonators [7], a large number of research papers have been published during the past 80 years with the aim of understanding the basic sound energy dissipation physics as well as improving impedance prediction models [6–21]. The acoustic energy damping mechanism strongly shifts from the viscosity within the orifice to acoustic-induced vortex shedding at the outlet side of the orifice or perforate opening. The dynamic energy of this unsteady vortex shedding is further dissipated by viscosity and thus improves the acoustic dissipation at high acoustic excitation levels. The process speeds up in the presence of bias flow, and losses are significantly increased since the flow sweeps away the shed vortices. Dean and Tester [22] proposed the bias flow concept as a method to control the impedance of turbofan inlet liners. Although the impact of bias flow on the impedance is very similar to the effect of high level acoustic excitation especially for the resistance part, the physics or flow pattern is quite different in that the non-linearity caused by high acoustic excitation is related to unsteady organized vortex shedding while the impact of bias flow is related to the turbulent flow around the orifice. Howe [23] presented an impedance model based on the Rayleigh conductivity for circular orifices with high bias flow speeds, which has been widely used in numerical simulations [24, 25]. There are not many published studies on the combination of high acoustic excitation and bias flow. Examples are analytical work in [26] and some experimental investigations in [27]. Studying such nonlinear phenomena requires numerical simulations and has in the past been shown to be time-consuming and sensitive to grid resolution [28] even without bias flow. Therefore, the motivation of our work is to experimentally gain a better understanding of the acoustic properties covering the cases ranging from those in which high-level nonlinear acoustic excitation is the factor determining the acoustic properties to the cases in which bias flow is most important, which physically relates to whether high-level acoustic excitation causes flow reversal in the orifice or whether the bias flow maintains the flow direction. The aim is also to provide a high-quality experimental database for the computational aeroacoustic (CAA) community.

In the second part of the thesis, the impedance of acoustic liners under grazing flow conditions is investigated. This work is directly motivated by the application of liners for inlets or outlets of aero engines with a strong grazing flow. Research on the influence of grazing flow has been gaining increasing interest since the 1950s. Quite a number of papers have been published, e.g. [29–36]. Although it has been known for many years that grazing flow affects the acoustic impedance of an orifice, the detailed mechanism of that influence is still under investigation. Generally, the acoustic resistance increases with increasing grazing flow, while reactance decreases. Theoretical models for the grazing flow effect on orifice impedance have been published which give a prediction of the general trend, but poor detailed validation against relevant experimental results [31–33]. Experimental results can vary compared to each other because of different setups, grazing flow boundary layer development and experimental techniques [34–38]. Different experimental techniques have been developed during the past years; examples are the in-situ technique developed by Dean [34] and the two-microphone method in [35, 36]. Both of them installed the microphones near an orifice or within cells of perforated liner structures. Several drawbacks and problems have been reported because of strong near-field effects. The two-microphone method may be influenced by higher-order mode wave propagation in cells since a plane wave assumption is required. Moreover, practical problem will be present for microphone installation in liner structures. Therefore, indirect impedance measurement techniques have been developed, so called impedance eduction tech-

niques, which move microphones outside of the liner and capture the acoustic signals far away from the liner. The impedance is identified as a boundary condition which is similar to the subsequent application in computational aeroacoustic (CAA) codes for engine noise prediction. These techniques have been initiated by NASA [37, 38] and over the last 20 to 30 years there have been many efforts to determine the relevant acoustic impedance under grazing flow conditions [37–55]. The acoustical waves in the experimental duct are normally computed combined with potential flow, while both the effect of the boundary layer of the grazing flow and the effect of the lined wall are taken into account as a boundary condition for the computation. The Ingard-Myers boundary condition [56] includes the effect of a lined impedance surface using the assumptions of continuity of acoustic normal displacement and pressure within the boundary layer. This concept has been used to develop methods for estimating the liner impedance from acoustic pressure measurements. One way is to use an iteration or minimization method where the experimental results are compared with simulated results starting from an initial impedance guess, see e.g. [37–41], or a faster straightforward method [42]. The measured acoustic information can vary from the sound pressure [48] to the measured transmission coefficients [49] and two-port matrix [55], or the velocity field [50]. For the simulation of sound propagation in the lined section and the connected hard walled ducts, different methods have been used, for instance, analytical solutions combined with the mode-matching method [40, 44] and finite difference method [48]. The identified impedance results could be influenced by many sources of error either from the numerical simulation, physical assumptions, or experimental errors. Examples are the initial impedance guesses for the closed loop minimization [41], the shear flow [45] and the Ingard-Myers boundary condition [47]. In order to improve the confidence, various comparison studies have recently been performed, using both different numerical methods [39, 43, 46] and different test rigs [53, 54]. The Ingard-Myers boundary condition has also attracted research attention in recent years, and a frequency-dependent parameter has been introduced for a transition from acoustic velocity continuity to displacement continuity within the boundary layer [47, 51]. The aim of the present work is to gain more confidence in the results based on a comparison with experiments from the German Aerospace Center(DLR), where the same locally reacting single-degree-of-freedom Helmholtz resonator liner sample was tested in two different test rigs. A numerical method is introduced for studying the influence of the flow and viscosity. Finally related systematic uncertainty is analyzed for the propagation of measurement errors.

Layout of the thesis

The thesis is organized as follows: Part I continues with Chapter 2 where the general theory of wave propagation in flow ducts is presented. Chapter 3 offers a review of the development of experimental techniques for flow ducts. Thereafter, in Chapter 4, experimental technology has been developed and a semi-analytical model is obtained for the combination effect of high acoustic excitation and bias flow. In Chapter 5, a systematic analysis for experimental impedance eduction techniques is given including: a comparative study of different methods from different test rigs, a numerical study for the effect of viscous and inviscid flow assumptions, and an experimental uncertainty analysis as well as a local Mach number discussion for the Ingard-Myers boundary condition. In Chapter 6, concluding remarks are presented and future work that may be worth considering is also discussed. Part I ends with a summary of appended papers. Part II contains the main results in the form of five papers. Two of them deal with acoustic properties on an in-duct orifice under high-level acoustic excitation and bias flow, while the other three systematically investigate the impedance eduction technique for grazing flow.

Chapter 2

Theory for wave propagation in flow ducts

In this chapter, fundamental theory for wave propagation in flow ducts is presented. Generally, wave propagation in viscous flow is governed by the compressible Navier-Stokes equations, and numerical simulation techniques are needed to solve these equations. Practically, due to the time-consuming calculation, a different simplified version is necessary. The acoustic wave equation is one of them, using a potential flow assumption. Analytical results can be found with a mode decomposition method. Higher-order mode waves are exponentially damped for low-frequency excitation, which makes the plane wave decomposition reasonable in the present study. For wave propagation in viscous shear flow, a linearized Navier-Stokes equations is presented.

2.1 Fundamental equations of fluid dynamics

Wave propagation in ducts with a real (viscous) laminar or turbulent flow is governed by the fundamental equations of fluid dynamics, the conservation law for mass, momentum and energy, called the Navier-Stokes equations. The continuity equation is given by

$$\frac{D\rho}{Dt} + \rho \frac{\partial u_i}{\partial x_i} = 0. \quad (2.1)$$

The momentum equation for Newtonian fluid (without body force) can be written as

$$\rho \frac{Du_i}{Dt} = -\frac{\partial p}{\partial x_i} + \frac{\partial \tau_{ij}}{\partial x_j}, \quad (2.2)$$

where τ_{ij} is the viscous stress tensor, which is defined as

$$\tau_{ij} = \mu \left(\frac{\partial u_i}{\partial x_j} + \frac{\partial u_j}{\partial x_i} - \frac{2}{3} \frac{\partial u_k}{\partial x_k} \delta_{ij} \right). \quad (2.3)$$

The energy equation is given by

$$\rho \frac{De}{Dt} = -p \frac{\partial u_k}{\partial x_k} + \tau_{ij} \frac{\partial u_i}{\partial x_j} + \frac{\partial}{\partial x_k} \left(\kappa \frac{\partial T}{\partial x_k} \right), \quad (2.4)$$

where u is the fluid velocity, ρ the density, p the pressure, T the absolute temperature, κ the thermal conductivity and e the internal energy, μ the dynamic viscosity and δ_{ij} the Kronecker delta. The material derivative is defined as

$$\frac{D}{Dt} = \frac{\partial}{\partial t} + u_j \frac{\partial}{\partial x_j}. \quad (2.5)$$

2.2 Wave propagation in ducts

In most cases, the Navier-Stokes equations can only be solved numerically and unfortunately the computation effort using direct numerical simulation is extremely time-consuming even with fast developing computation techniques. Therefore, simplifications are needed to give suitable solutions. The Helmholtz equation, for instance, can be derived for acoustic propagation. The flow quantities are split into a mean flow part and a perturbed small part. The energy equation Eq.(2.4) can be further simplified by assuming isentropic flow, and is written as

$$p' = c_0^2 \rho', \quad (2.6)$$

where the prime refers to a perturbed quantity, $c_0 = \sqrt{\gamma R_{\text{air}} T / M_{\text{air}}}$ is the adiabatic speed of sound, γ the ratio of specific heat, R_{air} the universal gas constant, and M_{air} the average molecular mass for air.

The control equations (2.1,2.2,2.6) can be simplified into the wave equation as

$$(\Delta^2 - \frac{1}{c_0^2} \frac{D^2}{Dt^2})p' = 0, \quad (2.7)$$

where Δ^2 is the Laplace operator. The flowing assumptions have been introduced:

- Ideal flow
- Homogeneous medium
- Isentropic relation between pressure and density
- Linear acoustics
- Uniform flow or stationary medium

2.2.1 Modal decomposition for waves in circular and rectangular ducts

The present study is limited to wave propagation in ducts, both circular and rectangular. For convenience, different coordinate systems can be adapted as shown in Fig. 2.1. The Laplace operator can be expressed in cylindrical coordinates as

$$\Delta^2 = \frac{1}{r} \frac{\partial}{\partial r} \left(r \frac{\partial}{\partial r} \right) + \frac{1}{r^2} \frac{\partial^2}{\partial \theta^2} + \frac{\partial^2}{\partial z^2}, \quad (2.8)$$

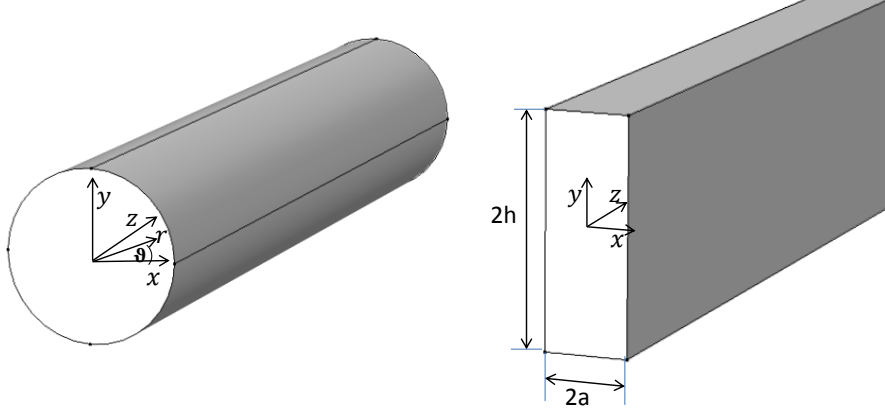


Figure 2.1: A circular duct and a rectangular duct with the cylindrical coordinate system (r, θ, z) and the Cartesian system (x, y, z)

with the axial coordinate z , the radial coordinate r , and the circumferential coordinate θ , and

$$\Delta^2 = \frac{\partial^2}{\partial x^2} + \frac{\partial^2}{\partial y^2} + \frac{\partial^2}{\partial z^2}, \quad (2.9)$$

in Cartesian coordinates.

2.2.1.1 Circular ducts

The wave equation in Eq. (2.7) can be solved with separation of variables and modal expansion. The pressure field can be written as a superposition of any infinite number of modes as

$$p'(t) = \sum_m \sum_n \hat{p}^{(m,n)} e^{j\omega t} \quad (2.10)$$

with the modes given as [4]

$$\hat{p}^{(m,n)}(r, \theta, z) = [\hat{p}_i^{(m,n)} e^{-jk_{zi}^{(m,n)} z} + \hat{p}_r^{(m,n)} e^{jk_{zr}^{(m,n)} z}] J_m(k_r r) e^{jm\theta}, \quad (2.11)$$

where the symbol $\hat{\cdot}$ is for a complex field, j is the imaginary unit, ω is the angular frequency, J_m is Bessel functions of the first kind. The subscripts i and r are for incident wave in the same direction as uniform flow and the reflected waves in the opposite direction. The subscripts $(m, n) \in \{0, 1, 2, \dots\}$ are integers for circumferential and radial mode orders. The axial wave number k_z is given by the relation for uniform flow as

$$\hat{k}_{zi,r}^{(m,n)} = \frac{k}{1 - M_0^2} [\mp M_0 + \sqrt{1 - (1 - M_0^2)(\frac{j_{mn}}{kR})^2}], \quad (2.12)$$

where $k = \omega/c_0$ is the wave number, - is for incident wave numbers $\hat{k}_{zi}^{(m,n)}$ and + for reflected wave numbers $\hat{k}_{zr}^{(m,n)}$; M_0 is for the mean(bulk) Mach number of the flow, and j_{mn} is the root of the derivative of Bessel functions J_m given by

$$J'_m(k_r R) = 0 \quad (2.13)$$

satisfying the rigid wall boundary conditions with R the radius of the duct and the radial wave number

$$k_r^{(m,n)} = \frac{j_{mn}}{R}. \quad (2.14)$$

Any mode (m, n) would propagate unattenuated if

$$1 - (1 - M_0^2) \left(\frac{j_{mn}}{kR} \right)^2 \geq 0, \quad (2.15)$$

or

$$kR \geq j_{mn} \sqrt{1 - M_0^2}. \quad (2.16)$$

2.2.1.2 Rectangular ducts

The wave equation Eq. (2.7), with the Laplacian given by Eq.(2.9) governs wave propagation in rectangular ducts. The modal contributions can be given as

$$\hat{p}^{(m,n)}(x, y, z) = [\hat{p}_i^{(m,n)} e^{-jk_{zi}^{(m,n)} z} + \hat{p}_r^{(m,n)} e^{jk_{zi}^{(m,n)} z}] \cos\left(\frac{n\pi(x+a)}{2a}\right) \cos\left(\frac{n\pi(y+h)}{2h}\right), \quad (2.17)$$

with mode shapes $\cos(\frac{n\pi(x+a)}{2a})$ and $\cos(\frac{n\pi(y+h)}{2h})$ satisfying the rigid wall boundary conditions at $x = \pm a$ and $y = \pm h$. The axial wave number is

$$\hat{k}_{zi,r}^{(m,n)} = \frac{k}{1 - M_0^2} [\mp M_0 + \sqrt{1 - (1 - M_0^2) [(\frac{m\pi}{2ka})^2 + (\frac{n\pi}{2kh})^2]}], \quad (2.18)$$

Any mode (m, n) would propagate unattenuated if

$$1 - (1 - M_0^2) [(\frac{m\pi}{2ka})^2 + (\frac{n\pi}{2kh})^2] \geq 0, \quad (2.19)$$

or

$$k \geq \sqrt{[(\frac{m\pi}{2a})^2 + (\frac{n\pi}{2h})^2] (1 - M_0^2)}. \quad (2.20)$$

The spatial distribution of the acoustic pressure is plotted in Fig.2.2. for the four modal components (m, n) (0,0), (1,0), (0,1) and (1,1) in both circular and rectangular ducts. The nodal lines of higher ($m > 1$ or $n > 1$) modal patterns are visible in the duct cross-section. Another characteristic feature of circular ducts is that the transversal pattern is rotating around the z -axis for higher ($m > 0$) circumferential modes, which are called spinning modes. This rotation phenomenon does not exist in rectangular ducts.

Eqs.(2.19,2.20) indicate a characteristic frequency where a mode starts propagating, i.e. the mode becomes cut-on. At this cut-on frequency, the terms on both sides of Eqs.(2.19,2.20) are equal, so that

$$f_c^{(m,n)} = \frac{j_{mn} c_0}{2\pi R} \sqrt{1 - M_0^2}, \quad (2.21)$$

or

$$f_c^{(m,n)} = \frac{c_0}{2\pi} \sqrt{[(\frac{m}{2a})^2 + (\frac{n}{2h})^2] (1 - M_0^2)}. \quad (2.22)$$

The cut-on frequency is dependent on the geometry of the duct cross-section, the mean flow Mach number, the speed of sound and the eigenvalue of the associated mode. A mode that is excited below its cut-on frequency is not able to propagate and is referred to as a cut-off

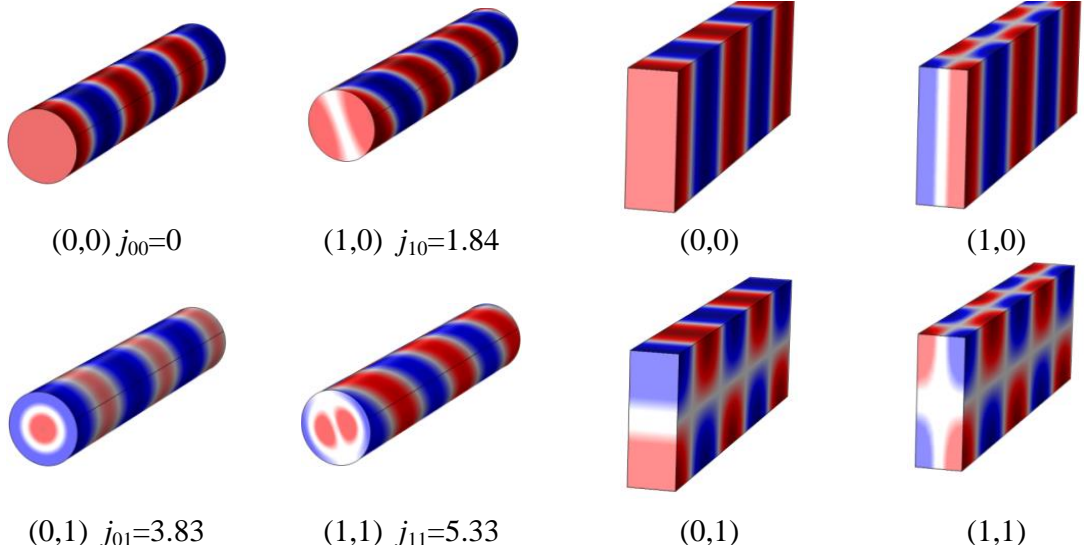


Figure 2.2: Illustration of acoustic pressure for four modal components (m,n) $(0,0)$, $(1,0)$, $(0,1)$ and $(1,1)$ in a cylindrical duct and a rectangular duct.

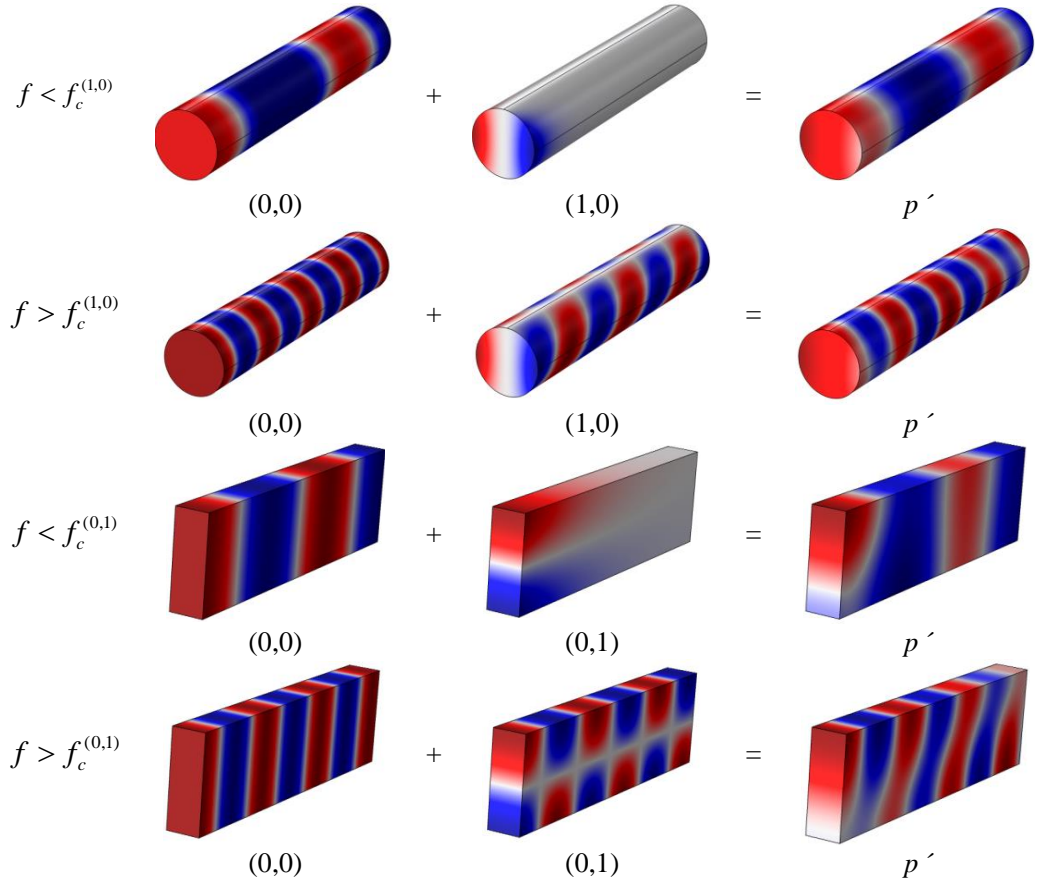


Figure 2.3: Illustration of cut-on phenomena of higher-order modes and the influence on the resulting sound field for mode $(1,0)$ for a circular duct and $(0,1)$ for a rectangular duct.

mode or evanescent mode. The amplitude decays exponentially, which is determined by the imaginary part of axial wave number $k_z^{(m,n)}$. The evanescent mode attenuation coefficient can be given by

$$\eta^{(m,n)} = \frac{2\pi}{c_0(1 - M_0^2)} \sqrt{|f^2 - f_c^{(m,n)2}|}. \quad (2.23)$$

At a given frequency f , only a limited number of modes are able to propagate and it is reasonable to neglect all evanescent modes, especially higher-order ones. However, evanescent modes might become important if the frequency is too close to the cut-on frequency, since the attenuation coefficient in Eq.(2.24) decreases when the frequency point is closer to the cut-on frequency. These evanescent mode waves cannot be neglected when the location of interest is in the vicinity of the source. Fig.2.3 illustrates the cut-on phenomenon with different frequency excitation, below the cut-on frequency and above the cut-on frequency. The acoustic pressure of the plane wave, the higher-order mode and the resulting sound pressure field are plotted.

2.2.2 Losses at the walls

Applying a no-slip boundary condition at a duct wall distorts the axial velocity sharply in the vicinity of the wall, which has not been considered in the wave equation. Furthermore, heat conductivity of the duct transfers acoustic energy into thermal energy, which is dissipated. The presence of turbulent flow could also interact with the propagating waves at certain frequencies. All these effects can be modelled and included in a complex wave number [4].

2.2.2.1 Wave number models for rigid walls

The effect of viscosity and heat conductivity of rigid walls has been studied as vorticity and entropy modes [4]. Theoretically, Kirchhoff [7] presented a wave number factor which was modified by Dokumaci [57] for cases with flow. Compared to acoustic waves in a stationary fluid, a mean flow in the duct modifies the wave numbers, slowing down upstream propagating waves, thus giving a shorter wavelength and speeding up downstream propagating waves, thus giving a longer wavelength. Real flow also induces additional damping of the waves because of viscosity, which in practical applications can be modeled by complex wavenumbers which are given by [57]

$$k_{zi,r} = \frac{kK_0}{1 \pm K_0M_0}. \quad (2.24)$$

where $+$ is for incident waves and $-$ for reflected waves, and K_0 is given by Kirchhoff [7] as

$$K_0 = 1 + \frac{1}{\sqrt{2}} \left[\frac{1-j}{s} \left(1 + \frac{\gamma-1}{\sqrt{\text{Pr}}} \right) \right] \quad (2.25)$$

with γ the ratio of specific heats, Pr the Prandtl number, $s = R\sqrt{\omega/\nu}$ the shear wavenumber, R the duct radius, and $\nu = \mu/\rho_0$ the kinematic viscosity. Obviously, these losses do not include the acoustic-turbulence interaction. Since the influence is limited to a specific range of frequencies $\omega\nu/U_\tau < 0.01$ [58] where U_τ is the friction velocity, this effect has not been included in the experimental study in the present thesis. More details can be found in [59].

2.2.2.2 Ingard-Myers boundary condition for lined walls

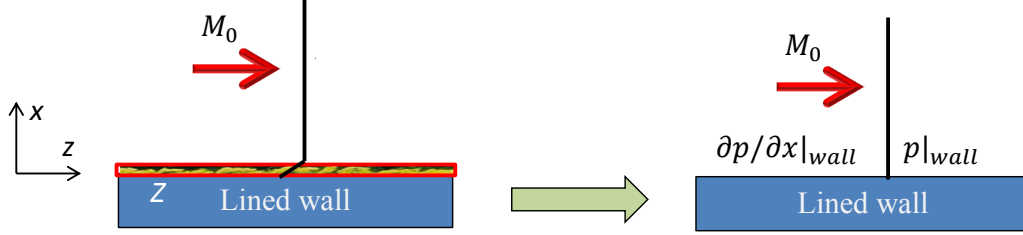


Figure 2.4: Illustration of Ingard-Myers boundary condition.

In contrast to the rigid wall, the lined wall is much more sensitive to the details of the flow close to the wall. It is difficult to give a general model considering the effect of the flow, where a thin turbulent boundary layer can modify the acoustic performance of the acoustic liner. The influence of vortex shedding near the wall treatment has been discussed for the last half century. Ingard [60] derived a boundary condition assuming continuity of the normal component of acoustic particle displacement for a planar boundary in a uniform axial mean flow field as show in Fig. 2.4. This assumption has been further extended by Myers [56] to non-uniform mean flow and lined walls with curvature, which can be expressed as

$$\partial \hat{p} / \partial x|_{\text{wall}} = \frac{jk}{Z} \left(1 - j \frac{M_0}{k} \frac{\partial}{\partial z}\right)^2 \hat{p}|_{\text{wall}}. \quad (2.26)$$

Viscosity is not considered in this assumption and recently some theoretical work on this issue has been done by Aurégan [61] and Brambley [62]. However, no unique model has been well accepted. Numerically, linearized Navier-Stokes equations can be used for investigating the shear flow and viscosity effect.

2.2.3 Linearized Navier-Stokes Equations (LNSE)

Wave propagation in a parallel shear flow with consideration of viscosity is governed by the linearized Navier-Stokes equations. These are a modified version of full compressible Navier-Stokes equations (Eqs.(2.1,2.2,2.6)), where the mean flow part and the perturbed part have been split and only linear terms are kept. A frequency domain linearized Navier-Stokes equation methodology [63] has proved to be efficient for cases where acoustic fields do not alter the mean flow field, i.e. when nonlinear phenomena like whistling do not occur. The present study focuses on wave propagation over a lined wall for studying the effect of shear flow and viscosity. In a two-dimensional duct with axial direction z and transversal direction x , a stationary problem is considered where all the fields and their derivatives are time harmonic with $e^{j\omega t}$. The linearized Navier-Stokes equations are given as below,

$$j\omega \hat{p} + U \frac{\partial \hat{p}}{\partial z} + \rho_0 \frac{\partial \hat{w}}{\partial z} + \rho_0 \frac{\partial \hat{u}}{\partial x} = 0, \quad (2.27)$$

$$j\omega \hat{w} + U \frac{\partial \hat{w}}{\partial z} + \hat{u} \frac{dU}{dx} = -\frac{1}{\rho_0} \frac{\partial \hat{p}}{\partial z} + \nu \left(\frac{4}{3} \frac{\partial^2 \hat{w}}{\partial z^2} + \frac{\partial^2 \hat{w}}{\partial x^2} + \frac{1}{3} \frac{\partial^2 \hat{u}}{\partial x \partial z} \right), \quad (2.28)$$

$$j\omega\hat{u} + U\frac{\partial\hat{u}}{\partial z} = -\frac{1}{\rho_0}\frac{\partial\hat{p}}{\partial x} + \nu\left(\frac{\partial^2\hat{u}}{\partial z^2} + \frac{4}{3}\frac{\partial^2\hat{u}}{\partial x^2} + \frac{1}{3}\frac{\partial^2\hat{w}}{\partial x\partial z}\right), \quad (2.29)$$

$$\hat{p} = c_0^2\hat{\rho}, \quad (2.30)$$

where $\hat{\rho}$, \hat{w} , \hat{u} are density, axial and transversal velocity perturbations. The shear flow velocity profile $U(x)$ is a function of x and ν is the kinematic viscosity.

Chapter 3

Experimental techniques for duct aeroacoustics

In this chapter, a review of experimental techniques for measuring liner impedance is given, starting from the standing wave tube method, over the two-microphone method and the impedance eduction technique of today. Furthermore, acoustic scattering matrix identification is introduced based on two-port theory.

3.1 Measurement techniques for determining impedance

The locally reacting assumption for acoustic liners has considerable advantages in simplicity for taking explicit account of the acoustic properties of surfaces. Experimentally, it simplifies the process of impedance measurement in that only one angle of wave incidence need be considered. The normal incidence acoustic impedance can be measured in several ways. Until now, most measurement techniques for determining liner impedance are implemented within ducts and based on a plane wave propagation assumption. As shown in section 2.2, higher-order mode waves attenuate exponentially and only plane waves can propagate for sufficiently low frequencies.

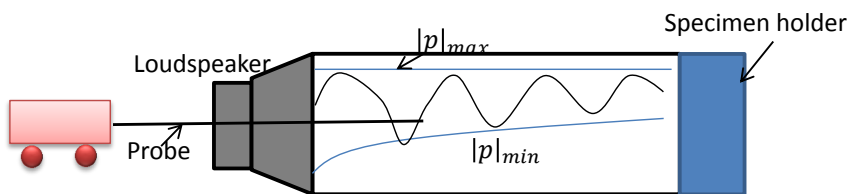


Figure 3.1: Schematic view of standing wave tube method.

The first known method is the standing wave tube method [64] as shown in Fig. 3.1 which has been commonly used for over 80 years. This method is based on the unique relationship between the standing wave parameters and the test specimen impedance. It is implemented with a moving pressure probe for measuring the distance of points with minimum and maximum pressure levels, as well as the standing wave ratio. This procedure was time-consuming and involved inaccuracy in the measurement of distance.

Since the 1970s, the development of signal analysis techniques, especially fast Fourier algorithms, provide the impedance measurement with a new possibility. Plane wave decom-

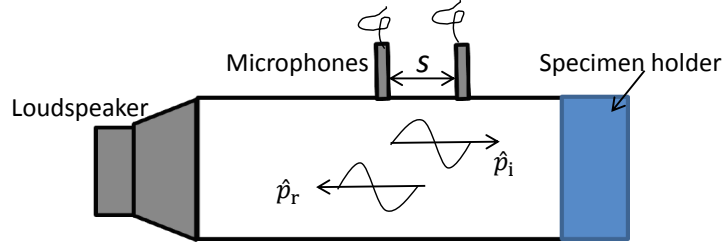


Figure 3.2: Schematic view of two microphone tube method.

position in the frequency domain enables the impedance measurement to be made much more easily with two microphones installed on the test tube, as shown in Fig. 3.2. The solution of the Helmholtz equation can be simplified as

$$p'(z, t) = \hat{p}_i e^{j(\omega t - k_{zi}z)} + \hat{p}_r e^{j(\omega t + k_{zr}z)}, \quad (3.1)$$

Basically, downstream propagating \hat{p}_i and upstream propagating waves \hat{p}_r can be decomposed with at least two microphones signals. Seybert and Ross [65] separated the incident and reflected wave spectra from measurements of auto- and cross-spectral densities between microphones, while Chung and Blaser [66] used the transfer function to determine the reflection coefficient of test specimens. The test tube can be adapted with different diameters to maintain plane waves at higher frequencies. This two-microphone technique has been used extensively and has become an ISO standard [67]. The influence of different types of measurement errors has been analysed and discussed by Åbom, Bodén [68, 69] and Schultz [70]. The distance of the two microphones, s , should be within a proper range, suggested by Åbom and Bodén as [69]

$$0.1\pi < \frac{ks}{1 - M_0^2} < 0.8\pi. \quad (3.2)$$

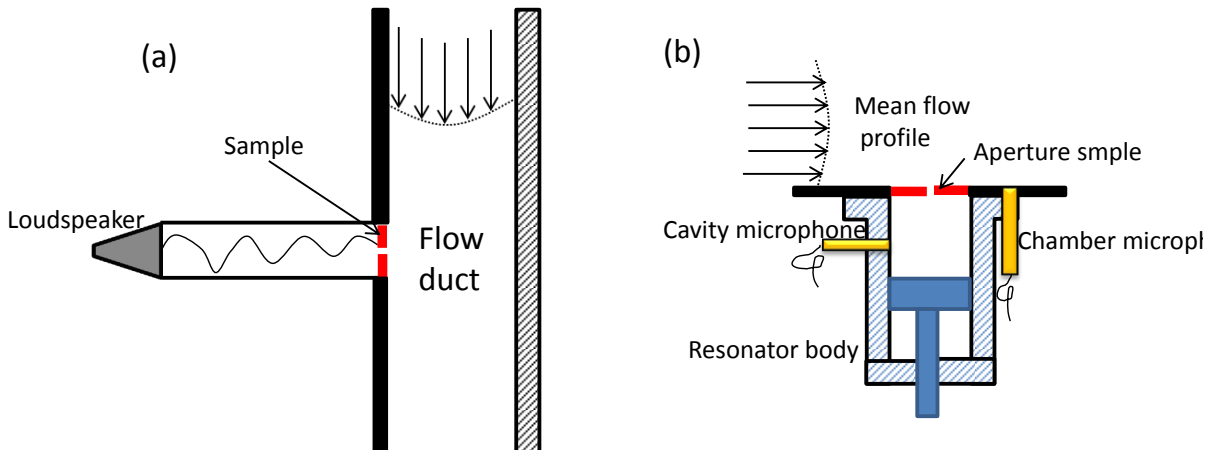


Figure 3.3: Orifice plate impedance measurement with shear flow. (a) standing wave tube-flow method by Mechel [71], (b) two-microphone method by Phillips [72].

In the presence of mean flow, both the standing wave tube and the two-microphone method have been applied for impedance of the aperture sample as shown in Fig. 3.3. Another

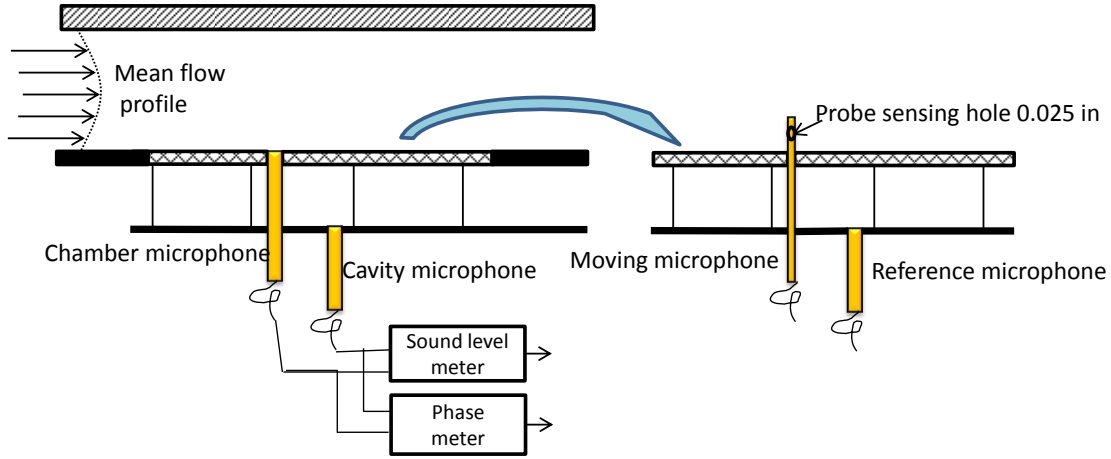


Figure 3.4: Locally reacting liner measurement with shear flow with two-microphone method-principle of operation and a modified version with the moving microphone probe by Dean [34].

very widely used method is called the in-situ technique as shown in Fig. 3.4 introduced by Dean[85]. It has been extensively used for determining impedance of locally reacting liners with or without flow. The method is based on the fact that for an acoustically compact resonant cavity liner, a simple relationship between cavity acoustic pressure and particle velocity exists and the particle velocities on either side of the cavity orifice are identical. It is assumed that the liner is locally reacting and the wavelengths are large compared to the cavity cross-dimensions. The quantities which are required are the acoustic pressure at any specified point in the cavity, the acoustic pressure at the surface and their phase difference. Usually, the transfer function from the microphone at the surface to the reference microphone installed in the cavity need to be further calculated. The microphone at the surface can be exchanged for a movable probe in order to obtain further acoustic pressure data in the test tube. Due to the compact installation, the in-situ method has some advantage over the two-microphone tube method. The pressure for impedance calculation is measured directly at the liner surface and does not rely on wave propagation within the test tube. Furthermore, it does not have a low frequency limitation under the cut-on frequency of plane wave in the test tube, which makes it possible to measure liner impedance under higher-order mode excitation. In principle, this in-situ technique can be carried out in a real engine during flight [73]. Some drawbacks and problems have also been noticed. The big issue is the influence of near fields or hydrodynamic fields with turbulent flow. Moreover, it is difficult to measure the liner with porous material in the cavity since there is no simple relationship between the particle velocity at the liner surface and the acoustic pressure in the cavity.

The continuing measurement challenge motivates the evolution of liner impedance measurement techniques in grazing flow environments. In order to get rid of the near field influence with an easier installation of pressure sensors, so-called impedance eduction techniques have been introduced, firstly by NASA Langley [37]. Fig. 3.5 shows the typical impedance eduction set-up. Instead of installing microphones near or within liner cells, the impedance eduction technique moves the sensors out of the near field of the liner region. They could be installed at the surface opposite to the liner sample or even far away upstream or downstream in rigid sections. They all rely on a mode of the wave propagation in the lined region. Quite

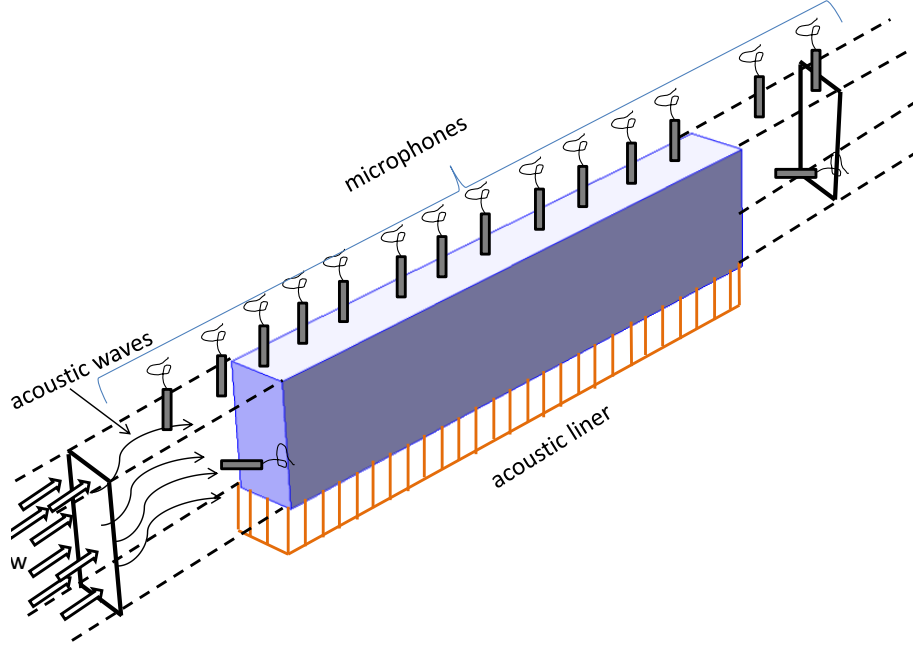


Figure 3.5: Illustration of typical impedance eduction set-up.

a number of different methods have been introduced and implemented based on different numbers of microphone clusters. For example, a solution for the wave propagation based on a numerical method such as the finite element method [52] can include as many microphones as possible, while the straightforward method based on Pronys method [42, 47] needs microphone data in the lined section with equidistant positions. The method based on a scattering matrix [55] or multi-mode matching method [44] basically requires only two clusters installed at the upstream and downstream sides. More details can be found in Chapter 5.

3.2 Scattering matrix identification based on two-port theory

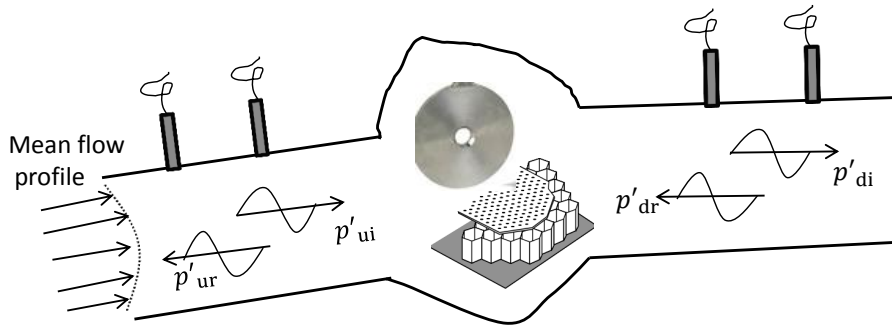


Figure 3.6: Forward and backward travelling plane wave components for acoustic properties of objects within a duct.

The scattering matrix is another way to qualify and access the acoustic performance of an

acoustic liner or any in-duct object. The objects studied are usually installed in the middle of a rigid tubes. Fig. 3.6 shows the two test objects studied in the thesis: one is an orifice and the other is an acoustic liner. Acoustic waves can be excited either from the upstream side or the downstream side. For upstream excitation, the sound source produces an incident plane wave, p'_{ui} , which travels towards the tested object and is scattered into a reflected, p'_{ur} , and transmitted wave. The waves propagating in the test object are scattered or partly absorbed, and further transmitted out with waves, p'_{di} . The transmitted wave is further reflected giving p'_{dr} at the outlet side of the test rig. The subscripts u, d refer to the inlet hard duct on the upstream side, d for the outlet hard duct on the downstream side.

Original two-port or four-pole theory comes from electrical network theory [74], which has been extended to any linear and time-invariant systems. In practical duct acoustics, it is an efficient way to characterize the acoustic performance in a plane wave frequency range. Different state parameters can be used [74], like pressure or particle velocity. Åbom [75] found that it is convenient to use pressure wave amplitudes as the state inputs and outputs, and the scattering matrix can be written as,

$$\begin{bmatrix} \hat{p}_{ur} \\ \hat{p}_{di} \end{bmatrix} = \mathbf{S} \begin{bmatrix} \hat{p}_{ui} \\ \hat{p}_{dr} \end{bmatrix}, \quad (3.3)$$

The scattering matrix has four elements given by

$$\mathbf{S} = \begin{bmatrix} R_1 & T_3 \\ T_1 & R_3 \end{bmatrix}, \quad (3.4)$$

where R_1 is the reflection coefficient at the upstream side, T_1 is the transmission coefficient in the direction from the upstream to the downstream side, and R_3, T_3 are the reflection and transmission coefficients at the opposite side or direction. To identify them, we need two sets of independent acoustic test cases. In the framework of small perturbations, which belongs to linear scattering matrix identification, either the two-load or two-source methods [76] can be used with any low level acoustic excitation for the identification. If the two-source method is used, we get

$$\begin{bmatrix} \hat{p}_{ur}^I & \hat{p}_{ur}^{II} \\ \hat{p}_{di}^I & \hat{p}_{di}^{II} \end{bmatrix} = \mathbf{S} \begin{bmatrix} \hat{p}_{ui}^I & \hat{p}_{ui}^{II} \\ \hat{p}_{dr}^I & \hat{p}_{dr}^{II} \end{bmatrix}, \quad (3.5)$$

where superscripts I, II stand for acoustic excitation from the upstream or downstream side.

Chapter 4

Characteristics of an in-duct orifice with bias flow under high-level acoustic excitation

This chapter discusses modelling, measurement techniques and results for an in-duct orifice with bias flow under high-level acoustic excitation. It starts with a review of an impedance model for a single degree-of-freedom liner. A harmonic method is proposed for modelling the phenomenon of the combination of bias flow and high-level acoustic excitation. The experimental setup is described and some measurement results are given.

4.1 Impedance model

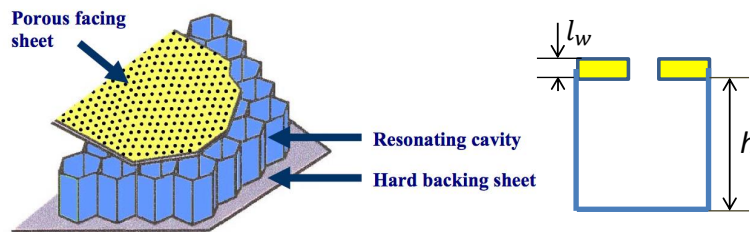


Figure 4.1: Honeycomb structure of a single degree-of-freedom (SDOF) liner and its equivalent model.

Fig. 4.1 shows a single degree-of-freedom Helmholtz resonator liner, which is locally reactive. The dimensions of orifices and cavities are much smaller than the wave length. The starting point is to model one cell of the liner structures as a perforated sheet backed with a cavity, so the normalized impedance can be modelled as a simple combination of perforated sheet impedance and cavity reactance. In order to derive the viscous impedance model for the orifice, micro-fluid phenomena are illustrated in Fig. 4.2. The fluid in and around the orifice moves back and forth driven by the acoustic pressure difference over the perforated plate. This attached fluid can be divided into two parts, the internal flow within the orifice and the outer part called attached mass. Outside of the orifice, a minimum flow area is called the vena contracta where streamlines are parallel. The flow from neighbouring orifices can be

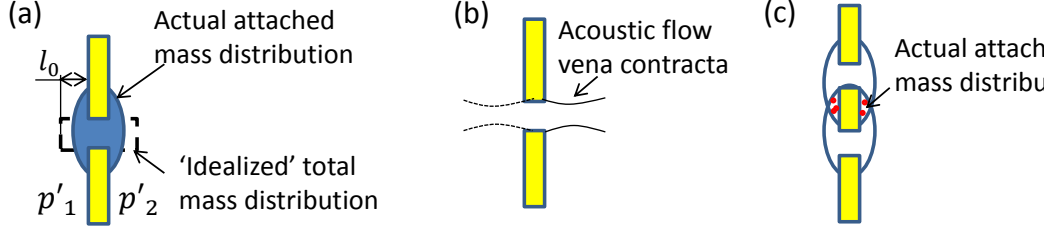


Figure 4.2: Schematic drawing of different micro-fluid phenomena in and around an orifice, (a) idealized and actual attached mass of air, (b) acoustic flow vena contracta, (c) interaction effects for the attached mass.

interactive if they are sufficiently close. Furthermore, in the presence of grazing or bias flow the micro-fluid movement can be influenced. Individually, these elements have been studied and a summary of normalized impedance model has been given by Elnady [77] mainly based on Crandall's theory [78], Bauer's model [79] and some empirical studies

$$Z_R = \text{Re}\left\{\frac{jk}{\sigma C_C} \left[\frac{l_w}{F(\mu')} + \frac{\delta_{re}}{F(\mu)} f_{int} \right] \right\} + \frac{1}{\sigma} \left(1 - \frac{2J_1(kd)}{kd} \right) + \frac{1 - \sigma^2}{\sigma^2 C_C^2} \frac{1}{2c_0} |\hat{V}| + \frac{0.5}{\sigma} M_g + \frac{1.15}{\sigma C_C} M_b, \quad (4.1)$$

$$Z_I = \text{Im}\left\{\frac{jk}{\sigma C_C} \left[\frac{l_w}{F(\mu')} + \frac{\delta_{im}}{F(\mu)} f_{int} \right] \right\} - \frac{1 - \sigma^2}{\sigma^2 C_C^2} \frac{1}{2c_0} \frac{|\hat{V}|}{3} - \frac{0.3}{\sigma} M_g - \cot(kh), \quad (4.2)$$

with

$$\mu' = \mu \left[1 + \frac{\gamma - 1}{\sqrt{\text{Pr}}} \right]^2, \quad (4.3)$$

$$K = \sqrt{-\frac{j\omega}{\nu}}, \nu = \frac{\mu}{\rho_0}, K' = \sqrt{-\frac{j\omega}{\nu'}}, \nu' = \frac{\mu'}{\rho_0}, \quad (4.4)$$

$$F(\mu) = 1 - \frac{4J_1(Kd/2)}{Kd \cdot J_0(Kd/2)}, \quad (4.5)$$

$$\delta_{re} = 0.2d + 300d^2 + 16000d^3, \quad (4.6)$$

$$\delta_{im} = 0.5d, \quad (4.7)$$

$$|\hat{V}| = \frac{|\Delta \hat{p}|}{\rho_0 c_0 \sqrt{Z_R^2 + Z_I^2}} \quad (4.8)$$

$$f_{int} = 1 - 1.47\sqrt{\sigma} + 0.47\sqrt{\sigma^3} \quad (4.9)$$

where Z_R and Z_I are normalized resistance and reactance, subscripts R and I stands for real and imaginary parts of a complex value, $|\cdot|$ means the absolute amplitude value, σ is the porosity converting the impedance of a single orifice into the impedance of an array of orifices in a perforation, C_C is the discharge coefficient describing the vena contracta, f_{int} is an empirical function for orifice hole interaction, l_w is the thickness of the orifice wall, d is the orifice diameter, h is the cavity depth, $\Delta \hat{p}$ is the pressure difference over the orifice, δ_{re} and δ_{im} are empirical end corrections for resistance and reactance, \hat{V} is acoustic velocity within the orifice hole for acoustic nonlinearity under high-level acoustic excitation, μ' is the effective value of viscosity considering the heat conductivity of orifice walls, ν and ν' are

kinetic viscosity and its effective value with hear conductivity of orifice walls, K and K' are the viscous Stokes wavenumber inside the hole, J_0 and J_1 are Bessel functions of the first kind, and M_g , M_b are Mach numbers for the grazing flow and the bias flow.

This model is only one of several models developed during the past years. For example, the end correction parameters δ_{re} , δ_{im} are individually studied for low-level acoustic excitation which is independent of acoustic excitation levels and bias flow, while the Cummings model [17, 18] indicates that the end correction should depend on acoustic velocity within the orifice holes and the discharge coefficient for acoustic flow is different from that for bias flow. The influence of bias flow is differently modelled by Howe [23] and Jing [80] based on the Strouhal number of bias flow instead of Mach number as here. More comparison studies can be found in Ref. [81]. The influence of grazing flow is still under investigation because of the influence of different set-ups and different turbulence boundary layers. More details are given in Chapter 5.

4.2 Nonlinear acoustic properties of an in-duct orifice with bias flow

4.2.1 The effect of combined high-level acoustic excitation and bias flow

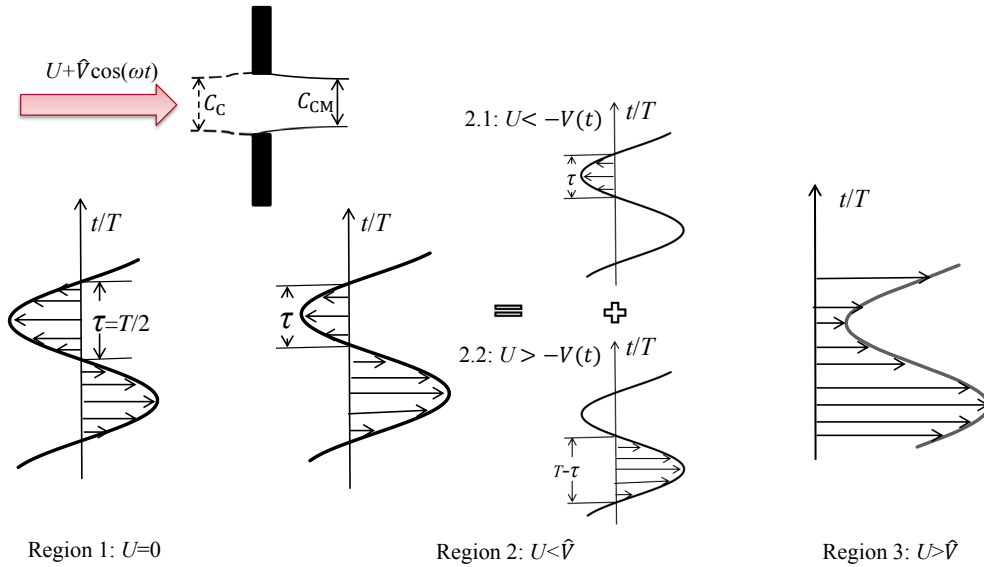


Figure 4.3: Flow directions through the orifice for different regions.

In the impedance model presented in section 4.1, it is assumed that the effect of flow and high-level acoustic excitation is additive without any interaction. It is, however, not always the case. One example is the effect of combined high-level acoustic excitation and bias flow. A simplified model of the steady flow through an orifice perturbed by a harmonic acoustic flow is presented in Fig. 4.3. At the edge of the orifice, a free jet can be formed by the separation of flow, which further contracts to a vena contracta, with a discharge coefficient

C_C for acoustic oscillating flow and C_{CM} for bias flow. For cases without flow under high-level acoustic excitation, the jet is unsteady and symmetric on both sides of the orifice while a steady jet exists only in the downstream side for high bias flow cases. This is related to whether high-level acoustic excitation causes flow reversal in the orifice or whether the bias flow maintains the flow direction, which is illustrated as Region 1 to Region 3 shown in Fig.4.3.

A possible way to derive an impedance model takes a starting point in the Cummings empirical equation based on the Bernoulli equation for unsteady flow, which is written as

$$l(t)\frac{dV(t)}{dt} + \frac{1}{2}\left(\frac{U+V(t)}{C_C(t)}\right)\left|\frac{U+V(t)}{C_C(t)}\right| = \frac{\Delta p'(t) + \Delta p_0}{\rho_0}, \quad (4.10)$$

where $l(t)$ is an effective orifice thickness including end corrections which can be time-varying, $V(t)$ is the fluctuating acoustic velocity in the orifice, U is the mean flow velocity. $p'(t)$ is the fluctuating pressure difference over the orifice, and $p_0(t)$ is the steady pressure drop over the orifice, and $C_C(t)$ is a discharge coefficient to consider the vena contracta effect which could also be time-varying.

The key parameters are the discharge coefficient and the effective orifice thickness. According to Cummings [82], the value 0.75 for discharge coefficient is consistent with experimental results for high-levels of acoustic excitation. In the presence of mean flow, the value of the discharge coefficient should vary according to the acoustic flow as well as mean flow velocity. Therefore, the discharge coefficient can be split into two parts: C_{CM} for mean flow and C_{CA} for acoustic flow. The discharge coefficient for mean flow can be easily found either from theory or experimental result. The acoustical flow discharge coefficient of an orifice can be equivalently determined as the average acoustic volume flow rate entering or exiting the orifice during a half-cycle. Hersh [15] experimentally studied the acoustic flow discharge coefficient of the orifice for a Helmholtz resonator and observed that it tended to be unity at low acoustic excitation levels and decreasing with an increase of acoustic excitation. It also followed from the numerical investigations of Zhang [28], which, in addition, showed that the discharge coefficient increased with frequency at a constant acoustic excitation level. However, both studies were limited to cases without mean flow where acoustic flow determines the acoustic properties as in Region 1. In the presence of mean bias flow as in Region 2, the flow reversal part shown in Region 2.1 should have a similar effect to that of acoustic flow and one can expect the acoustic flow discharge coefficient to depend on the total velocity. In regional 2.2 where bias flow maintains the direction, the flow discharge coefficient should be in-between the mean flow discharge coefficient and the minimum acoustic flow discharge coefficient for fully developed turbulent acoustic flow.

The effective orifice length $l(t)$ describes the acoustic inertia of the irrotational flow around orifices. Assuming that the irrotational flow is mainly within and downstream of the orifices, an empirical expression for the time-varying effective orifice length was presented by Cummings [17] as

$$l(L_J) = l_0 + \frac{l_w + l_0}{1 + \frac{(L_J/d)^{1.585}}{3}}, \quad (4.11)$$

where $l_0 \approx (\pi/8) \cdot d$ is the end correction on one side of the orifice, and $L_J(t)$ is a time-varying jet length caused by the high-level acoustic excitation. Cummings suggested that

the jet length should be estimated from

$$L_J(t) = \int_{\tau_J} |U + V(t)| dt, \quad (4.12)$$

where τ_J is the jet age from the beginning of the acoustic half cycle to where $V(t)$ changes sign, which means τ_J equals half a period of acoustic flow in the absence of mean flow. Following the discussion in [26], the jet length could be much more complex, especially when flow reversal occurs. The average effective length (\bar{l}) should tend to have a maximum value ($l_w + 2l_0$) under low acoustic excitation without mean flow, and have a minimum value (l_0) either for high acoustic excitation or with high mean flow.

Under these considerations, an acoustic impedance model is built in Paper II based on a harmonic balance analysis of the Cummings equation for the different regions described in Fig. 4.3.

Region 1 ($U=0$):

$$Z(\omega) = \frac{4}{3\pi} \frac{\hat{V}}{c_0 C_{CA1}^2} + j \cdot \frac{\omega}{c_0} l(L_{J1}), \quad (4.13)$$

where

$$C_{CA1} = 1 - (1 - C_{CAmin}) \cdot \operatorname{erf}\left(\frac{\sqrt{\pi}}{4000 C_{CAmin}} \frac{V_{rms1}^2}{\omega \nu}\right), V_{rms1}^2 = \frac{\hat{V}^2}{2}, \quad (4.14)$$

$$l(L_{J1}) = l_0 + \frac{l_w + l_0}{1 + \frac{(L_J/d)^{1.585}}{3}}, L_{J1} = \frac{2\hat{V}}{\omega}. \quad (4.15)$$

Region 2 ($U \leq \hat{V}$):

$$Z(\omega) = \frac{1}{2\pi c_0 \hat{V}} \left[\frac{(\sin 3\theta + 9\sin\theta)\hat{V}^2}{6C_{CA2}^2} + \frac{(\sin 3\theta + 9\sin\theta)\hat{V}^2}{6C_{CA3}^2} - \frac{(2\theta + \sin 2\theta) \cdot U\hat{V}}{C_{CA2}C_{CM}} \right. \\ \left. + \frac{(2\pi - 2\theta - \sin 2\theta) \cdot U\hat{V}}{C_{CA3}C_{CM}} + \frac{4\sin\theta \cdot U^2}{C_{CM}^2} \right] + j \cdot \frac{\omega}{c_0} \bar{l}, \quad (4.16)$$

where

$$C_{CA2} = 1 - (1 - C_{CAmin}) \cdot \operatorname{erf}\left(\frac{\sqrt{\pi}}{4000 C_{CAmin}} \frac{V_{rms2}^2}{\omega \nu}\right), \quad (4.17)$$

$$V_{rms2}^2 = \frac{\hat{V}^2}{2} + U^2 + \frac{1}{\theta} \left[\frac{\sin 2\theta \cdot \hat{V}^2}{4} - 2U\hat{V}\sin\theta \right], \quad (4.18)$$

$$C_{CA3} = C_{CM} - (C_{CM} - C_{CAmin}) \cdot \operatorname{erf}\left(\frac{\sqrt{\pi}}{4000 C_{CAmin}} \frac{V_{rms3}^2}{\omega \nu}\right), \quad (4.19)$$

$$V_{rms3}^2 = \frac{\hat{V}^2}{2} + U^2 - \frac{1}{\pi - \theta} \left[\frac{\sin 2\theta \cdot \hat{V}^2}{4} - 2U\hat{V}\sin\theta \right], \quad (4.20)$$

$$\theta = \arccos(U/\hat{V}). \quad (4.21)$$

Region 3 ($U > \hat{V}$):

$$Z(\omega) = \frac{U}{c_0 C_{CM} \cdot C_{CA4}} + j \cdot \frac{\omega}{c_0} \bar{l}, \quad (4.22)$$

where

$$C_{CA4} = C_{CM} - (C_{CM} - C_{CAmin}) \cdot \operatorname{erf}\left(\frac{\sqrt{\pi}}{4000C_{CAmin}} \frac{V_{rms4}^2}{\omega\nu}\right), V_{rms4}^2 = \frac{\hat{V}^2}{2}. \quad (4.23)$$

where θ is an index for different combinations of bias flow and high acoustic excitation levels, C_{CM} is mean flow discharge coefficient, C_{CAmin} is the minimum acoustic flow discharge coefficient for fully developed turbulent acoustic flow, C_{CA1} , C_{CA2} , C_{CA3} and C_{CA4} are different discharge coefficient models for different regions, and the error function $\operatorname{erf}(x) = (2/\sqrt{\pi}) \int_0^x e^{-\xi^2} d\xi$ controls the change of discharge coefficients. Fig. 4.4 shows the change of values of discharge coefficient with effective mean acoustic velocity V_{rms} .

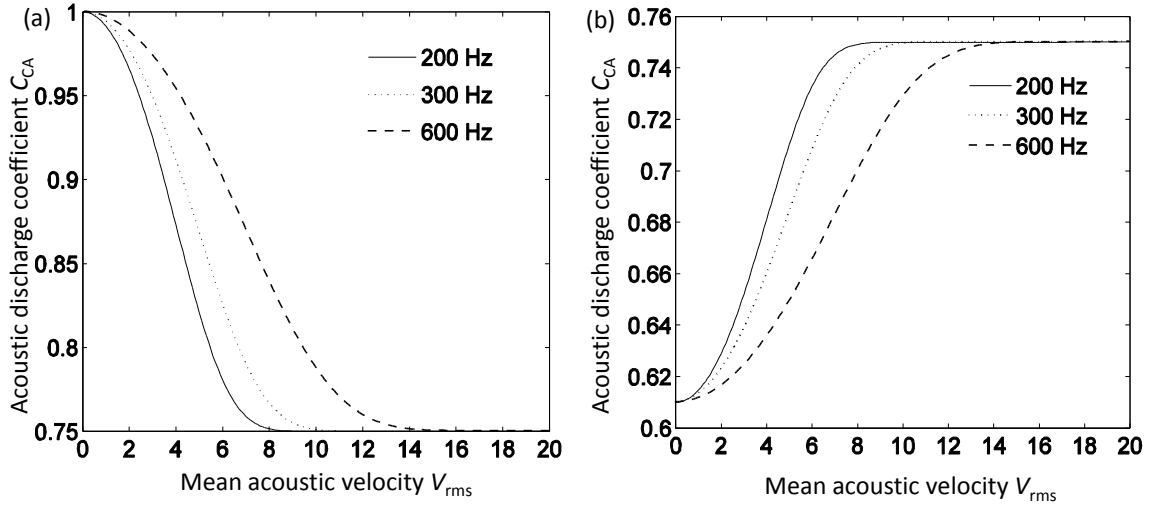


Figure 4.4: Acoustic discharge coefficient as a function of mean acoustic velocity and frequency: (a) no mean flow, (b) with mean flow ($C_{CM} = 0.61$, $C_{CAmin} = 0.75$).

4.2.2 Nonlinear scattering matrix and energy dissipation/generation

Consider a small orifice installed between two uniform pipe segments as shown in Fig. 4.5. Low porosity gives relative high acoustic flow velocity in the orifice while it is much lower in the main pipe so that any nonlinear acoustic effects are confined to the orifice region. It is therefore assumed, supported by experimental evidence, that nonlinear propagation effects in the main pipe can be neglected. For low frequencies, the thickness of the orifice is small compared with the wavelength and one can assume that the acoustic velocity is the same on both sides, which gives the following transfer matrix

$$\begin{bmatrix} \hat{p}_u \\ \hat{V}_u \end{bmatrix} = \begin{bmatrix} 1 & \rho_0 c_0 Z \\ 0 & 1 \end{bmatrix} \begin{bmatrix} \hat{p}_d \\ \hat{V}_d \end{bmatrix}, \quad (4.24)$$

with $\hat{p}_u = \hat{p}_{ui} + \hat{p}_{ur}$, $\hat{p}_d = \hat{p}_{di} + \hat{p}_{dr}$ for complex pressure values at the upstream and downstream side, and \hat{V}_u , \hat{V}_d for the acoustic velocities. The Normalized impedance and acoustic particle velocity are given by

$$Z = \frac{\hat{p}_u - \hat{p}_d}{\rho_0 c_0 \hat{V}_u}, \quad (4.25)$$

$$\hat{V}_u = \frac{\hat{p}_{ui} - \hat{p}_{ur}}{\rho_0 c_0 \sigma}, \hat{V}_d = \frac{\hat{p}_{di} - \hat{p}_{dr}}{\rho_0 c_0 \sigma}, \quad (4.26)$$

Substituting into Eq.(4.24) the scattering matrix (Eq.(3.3)) of the orifice can be expressed in terms of impedance as

$$\mathbf{S} = \frac{1}{2 + Z/\sigma} \begin{bmatrix} Z/\sigma & 2 \\ 2 & Z/\sigma \end{bmatrix}, \quad (4.27)$$

For the linear region, the scattering matrix can be identified with any combinations of two independent acoustic excitations as Eq.(3.5). However, for the nonlinear region, an additional condition which should be added is to keep the same magnitude of acoustic pressure difference or the same magnitude of acoustic flow velocity in the orifice. It can be expressed as

$$|\hat{p}_u^I - \hat{p}_d^I| = |\hat{p}_u^{II} - \hat{p}_d^{II}|, \quad (4.28)$$

where $\hat{p}_u^{I,II} = \hat{p}_{ui}^{I,II} + \hat{p}_{ur}^{I,II}$, $\hat{p}_d^{I,II} = \hat{p}_{di}^{I,II} + \hat{p}_{dr}^{I,II}$.

In order to analyse the energy dissipation or generation, a Hermitian energy dissipation matrix $\mathbf{I} - \mathbf{S}^* \mathbf{S}$ can be mathematically transformed into a diagonal matrix of its eigenvalues (ξ_1, ξ_2) and eigenvectors $\mathbf{Q}_1, \mathbf{Q}_2$. These eigenvalues are indicators for the potentiality of acoustic dissipation or generation [73]. If $\min\{\xi_1, \xi_2\} > 0$, acoustic energy will be dissipated and the orifice system is acoustic passive; if $\min\{\xi_1, \xi_2\} < 0$ and $\max\{\xi_1, \xi_2\} > 0$, acoustic energy will be dissipated or produced, depending on the actual acoustic excitation pattern, which can be decomposed into a combination of eigenvectors:

$$\begin{bmatrix} \hat{p}_{ui} \\ \hat{p}_{dr} \end{bmatrix} = a_1 \mathbf{Q}_1 + a_2 \mathbf{Q}_2. \quad (4.29)$$

Paper I shows that the energy absorption can be given as $|a_1|^2 \xi_1 + |a_2|^2 \xi_2$. The system is conditionally passive dependent on the sign of $|a_1|^2 \xi_1 + |a_2|^2 \xi_2$. If $\max\{\xi_1, \xi_2\} < 0$ acoustic energy will be generated and the systems is active. Theoretically the minimum/maximum potentially dissipation coefficient can be calculated from Eq.(4.27)

$$\xi_1 = 0, \xi_2 = \frac{4(Z^* + Z)/\sigma}{(2 + Z/\sigma)^*(2 + Z/\sigma)} \quad (4.30)$$

with $*$ denotint complex conjugation and the corresponding eigenvectors or mode shapes $\mathbf{Q}_1 = [\sqrt{2}/2; \sqrt{2}/2]$ and $\mathbf{Q}_2 = [\sqrt{2}/2; -\sqrt{2}/2]$. No energy can be dissipated or generated if incident waves from upstream (\hat{p}_{ui}) and downstream (\hat{p}_{dr}) act in phase with the same amplitude, and there is no acoustic pressure difference over the orifice ($\hat{p}_u = \hat{p}_d$). Maximum energy can be dissipated or generated if incident waves act in anti-phase with the same amplitude, and the acoustic pressure difference becomes maximum. Whether acoustic energy will be dissipated or generated depends on the orifice resistance, which means that for the resistance $\text{Re}(Z) > 0$, there is a positive eigenvalue and the acoustic energy is dissipated; while for $\text{Re}(Z) < 0$, the eigenvalue is negative and the acoustic energy is generated.

4.3 Experimental setup

The experimental setup is illustrated in Fig. 4.5. The test object is an orifice plate mounted in a duct with a diameter of 40 mm. Six microphones were divided into two groups and symmetrically installed on both sides of the test sample so that the two-microphone wave decomposition method could be used to identify the sound wave components on each side. Two different transducer separations (24 mm and 180 mm) gave a frequency range from 80Hz up to 5000Hz. On both sides, high quality loudspeakers were mounted as the excitation source. For the acoustic impedance identification tests, only the loudspeaker on the upstream side was used, while both were used for the nonlinear scattering matrix identification. The acoustic excitation levels were controlled so that the amplitude of oscillating velocity in the orifice(\hat{V}) could be kept constant. Compared to the in-orifice hot-wire measurements in Ref. [10, 21] this velocity represents an average over the orifice rather than only a single point value. Pure tone acoustic excitation was used and it was checked that higher order nonlinear harmonics were sufficiently small when performing high excitation level measurements. In order to measure the mean flow velocity in the orifice(U), on the upstream side, a laminar flow meter (2000 SLPM, Alicat Scientific, Inc.) was employed during the experiment. It converts the mass airflow to a voltage signal with a range between 0 V (0 SLPM) and 5 V (2000 SLPM). The sensor linearity has been calibrated by the manufacturer. A sound attenuation system, including a tunable Helmholtz resonator and a muffler, was designed to attenuate the sound to less than 126 dB at the position of the laminar flow meter, to reduce the measurement error caused by the fluctuating flow. During the experiment, the steady pressure drop over the orifice(Δp) was also monitored by two pressure sensors installed further away from the

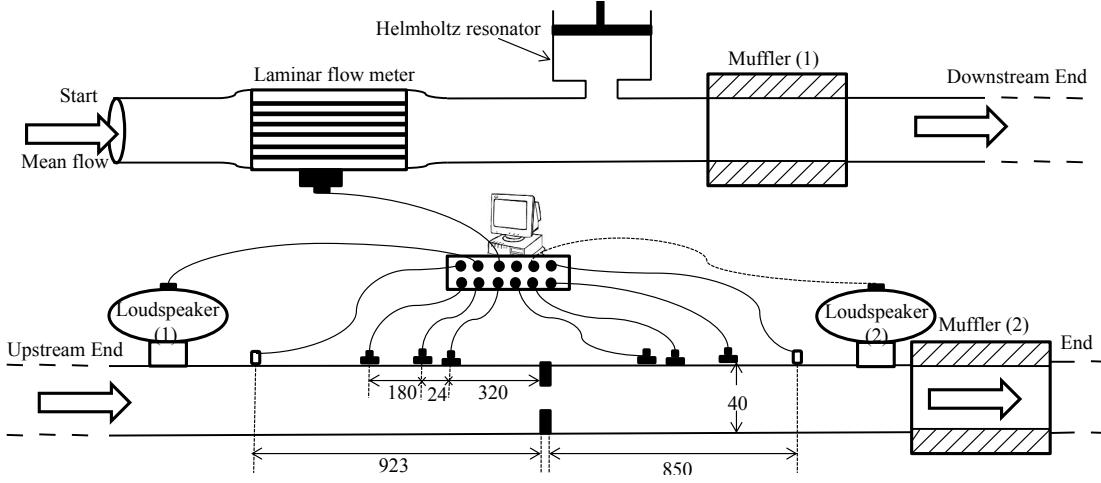


Figure 4.5: Schematic of the experimental setup, dimensions in millimetres.

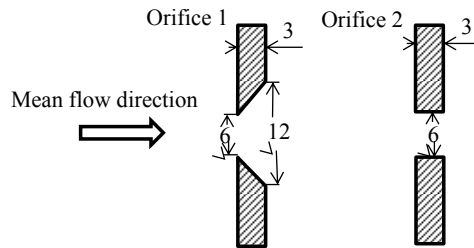


Figure 4.6: Orifice geometry, Orifice1: chamfer-edged, Orifice 2: thick sharp-edged.

test sample than the microphones. These pressure sensors were carefully calibrated with a pressure calibrator. The signals from both the laminar flow meter and the pressure sensors were recorded together with the signals from microphones using a NI LabVIEW Real-Time Module. The mean values for flow velocity(U) and static pressure drop(Δp) were averaged for a 3-5s long stable signal. The mean flow discharge coefficient(C_{CM}) could be calculated as

$$C_{CM} = \frac{U}{\sqrt{2\Delta p/\rho_0}}. \quad (4.31)$$

In the study, a wide range of mean flows (0-19m/s in the orifice), sound levels (100-155dB) and frequencies (100-1000Hz) were considered. Two orifice plates were tested, which have the same thickness and hole diameter, but different edge geometries, as shown in Fig.4.6. Orifice 1 does not have a perfect sharp edge on the upstream side. Instead, it has an equivalent thickness about 0.6 mm for the hole with a diameter of 6 mm. The main part of the study was conducted by using orifice 2. Orifice 1 was added to illustrate the effect of a small equivalent thickness on flow instability.

4.4 Some results and discussion

4.4.1 Impedance results

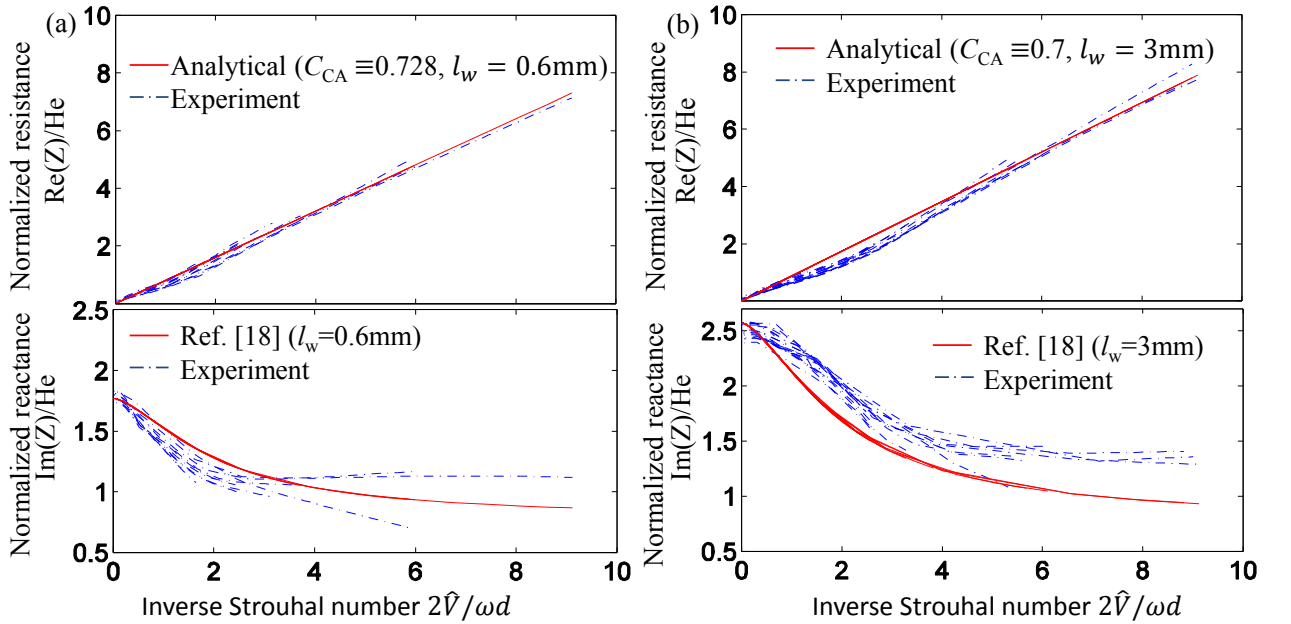


Figure 4.7: Normalized acoustic impedance divided by Helmholtz number ($\omega d/2c_0$) plotted against inverse Strouhal number ($2\hat{V}/\omega d$), without bias flow, frequency range: 100-1000Hz, (a): Orifice 1, (b): Orifice 2.

Fig. 4.7 shows the normalized impedance divided by the Helmholtz number without bias flow, which makes the curves for different frequencies collapse. There is a fairly good agreement between experimental resistance and the analytical results from Eq.(4.13) even when the discharge coefficients are kept as a constant minimum value, which is 0.728 for Orifice 1 and 0.7 for Orifice 2. For acoustic reactance with the Cummings' effective orifice

length model, the analytical results have a qualitative consistency with our experimental results as shown in Fig.4.7. The experimental results show that the reactance has a constant value with $l = l_w + 2l_0$ at low acoustic levels; decreases with higher acoustic excitation levels; and tends to a constant level with a small value at high excitation levels. This minimum reactance value seems to vary with different orifice geometries. The mechanism causing the decrease in mass reactance can be considered as an energy transfer from reactive acoustic energy stored by the inertial mass in and around one side of the orifice to turbulent motion. This energy is thus sooner or later dissipated by viscosity causing an increase of the nonlinear resistance. However, the transfer seems to have a limitation where the mass reactance does not become smaller than the end correction on one side, while the resistance keeps increasing.

Table 4.1: Measured bias flow velocity and mean flow discharge coefficient

Orifice1				Orifice2			
Bias velocity $U(\text{m/s})$	flow $U(\text{m/s})$	Reynolds number Ud/ν	Discharge coefficient C_{CM}	Bias velocity $U(\text{m/s})$	flow $U(\text{m/s})$	Reynolds number Ud/ν	Discharge coefficient C_{CM}
2.8		1084	0.663	3.9		1510	0.799
7.8		3019	0.676	7.4		2865	0.610
11.5		4452	0.697	11.7		4529	0.687
				14.5		5613	0.645
				18.6		7200	0.684

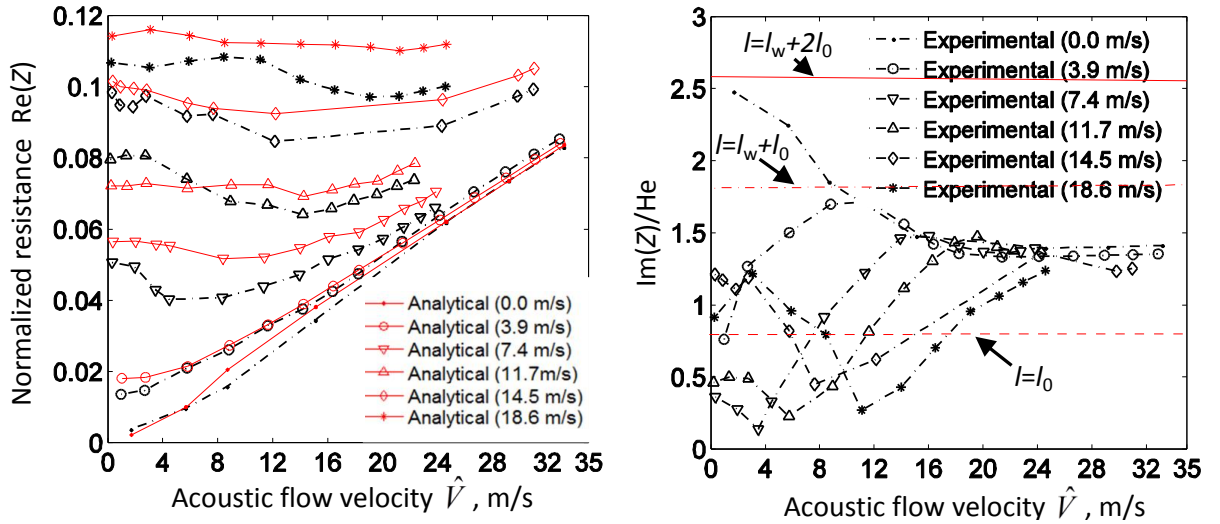


Figure 4.8: Normalized acoustic impedance for different bias flow velocities, Orifice 2, frequency: 200Hz.

Different bias flow cases have been considered as shown in Table. 4.1 and the mean flow discharge coefficient has been calculated from measured pressure drop. Fig. 4.8 compares acoustic impedance results for orifice 2 with different bias flow velocities and acoustic excitation levels varying from low to high, which is from Region 3 ($U > \hat{V}$) to Region1($U = 0$ or $U \ll \hat{V}$) according to Fig. 4.3. The results show that the acoustic resistance firstly decreases with an increase in acoustic excitation level, and then tend to increase and approach the result without bias flow. The minimum is obtained when the acoustic velocity is

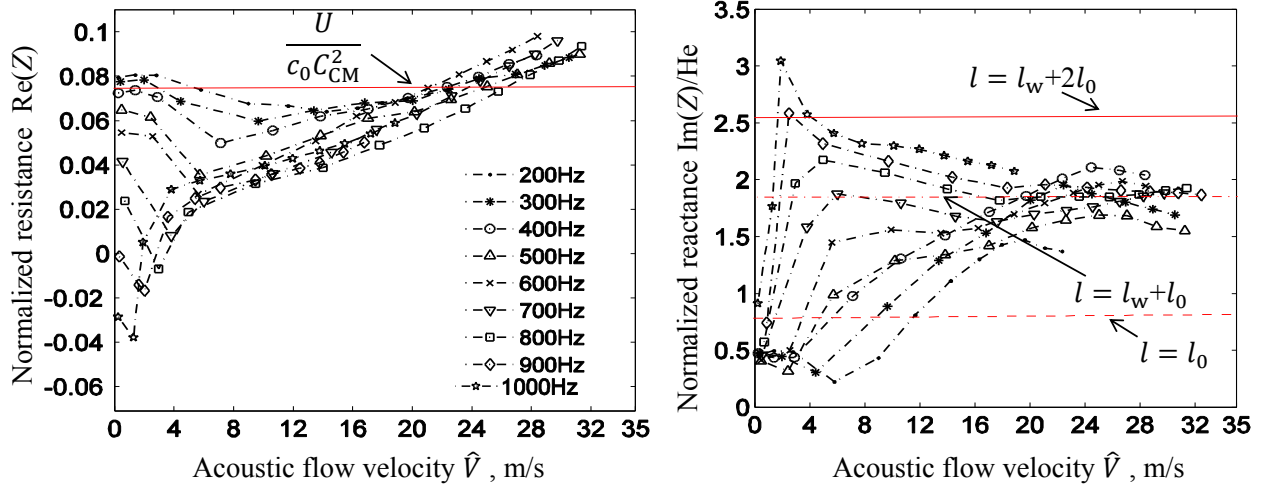


Figure 4.9: Normalized acoustic impedance for different frequencies, Orifice 2, $U=11.7$ m/s.

similar in magnitude to the bias flow velocity. The reason could be related to the difference in values of mean flow discharge and acoustic discharge coefficient, since normally the acoustic discharge coefficient is a bit larger than the mean flow discharge coefficient, as validated from the fairly good agreement with analytical results. The reactance, which is plotted divided by the Helmholtz number, has varying values for low acoustic excitation depending on mean flow velocity and orifice geometries. The values are even smaller than the one-sided end correction for relative high bias flow levels. Compared with the no bias flow case, even a very small bias flow can decrease the reactance substantially for low acoustic excitation levels. With increase of acoustic excitation, the acoustic reactance starts to increase to a maximum value. Then it behaves similarly to that in the no bias flow cases. This transfer point for acoustic flow velocity depends on the bias flow velocity. The higher the bias flow velocity, the higher the acoustic excitation it needs.

There is no doubt that acoustic impedance is also frequency-dependent. Fig. 4.9 shows the values of acoustic impedance for different frequencies with the same bias flow velocity for orifice 2. For Region 3 ($U > \hat{V}$), low frequencies and low acoustic excitation, the value for resistance is quite close to the analytical result, which is dependent on bias flow velocity and mean flow discharge coefficient. In this case, the flow jet kinetic energy changes slowly. So the flow discharge coefficient should be quite stable and close to the value in the absence of acoustic excitation, which was measured and used for the analytical model. For higher frequencies, the dimension of unsteady vorticity outside of the incompressible jet should be in the order of magnitude $\sim U/\omega$, which means the scale of turbulence decreases with frequency. Therefore, additional irrotational flow is developed and the flow discharge coefficient increases with the vena contracta area expansion, which means that the mean flow discharge coefficient could also depend on frequency. The resistance for some high frequencies even decreased to a negative value and the reactance sharply increased at low acoustic excitation. The reason is that these frequencies (800-1000Hz) fall into the range of flow instability, where the Strouhal number based on orifice thickness and bias flow (fl_w/U) equals 0.2-0.35 [83]. Increasing acoustic excitation increases the resistance to positive values for these cases, which means the high acoustic level can decrease the flow instability.

4.4.2 Energy dissipation/generation

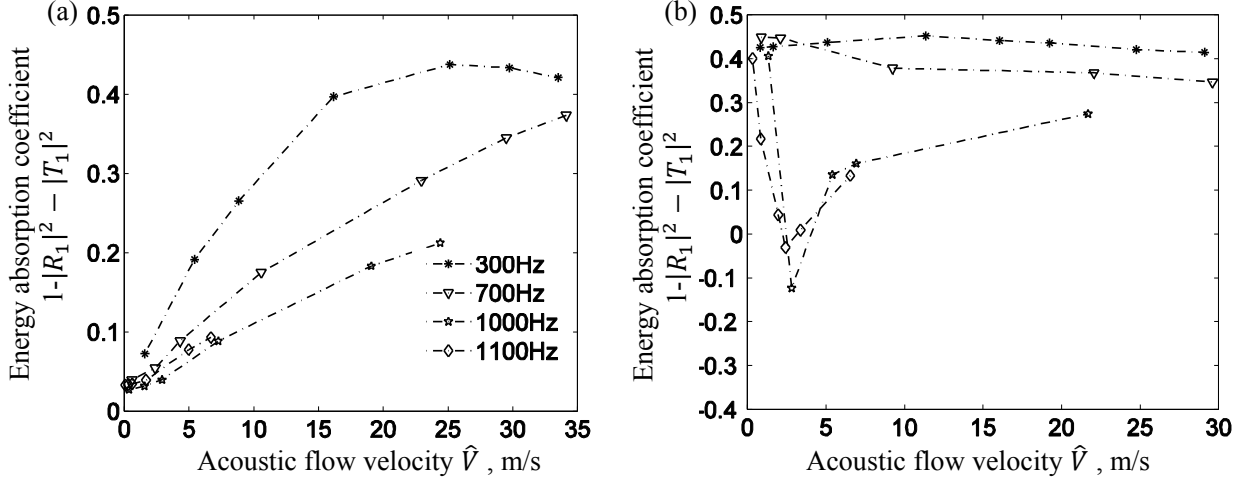


Figure 4.10: Energy absorption coefficient for upstream excitation ($|\cdot|$ for absolute value and R_1, T_1 are reflection and transmission coefficient for upstream acoustic excitation), Orifice 2, (a): $U = 0$ m/s, (b): $U = 14.5$ m/s.

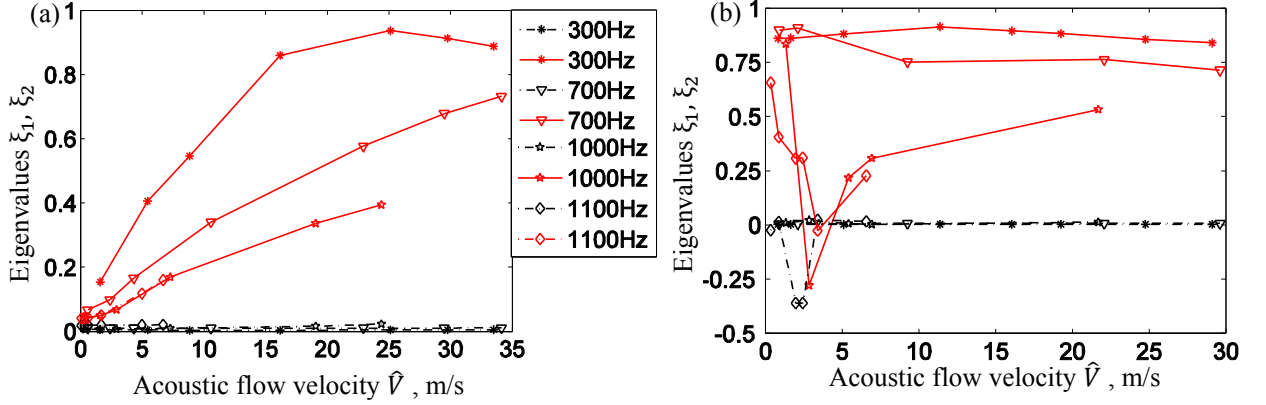


Figure 4.11: Eigenvalues of dissipation matrix $\mathbf{I} - \mathbf{S}^*\mathbf{S}$ representing the minimum/maximum ratio of potential dissipated acoustic power, Orifice 2, ξ_1 -red lines, ξ_2 -black lines. (a): $U = 0$ m/s, (b): $U = 14.5$ m/s.

In order to investigate the energy dissipation, a nonlinear scattering matrix is identified using the two-load method [76]. Loudspeaker levels were finely controlled in order to keep the same level of nonlinearity as Eq. (4.28). Fig. 4.10 shows the energy absorption coefficient for upstream excitation and the energy dissipation potentiality is shown in Fig. 4.11 in terms of eigenvalues of the dissipation matrix $\mathbf{I} - \mathbf{S}^*\mathbf{S}$. Without bias flow, higher level acoustic excitation increases the acoustic energy dissipation especially for low frequencies as shown in Fig. 4.10(a). Fig. 4.10(b) shows that bias flow can also greatly increase the dissipation for low and medium acoustic excitation at frequencies far from flow instability. The unstable flow region, where the energy absorption coefficients tend to be negative, coincides with the region of negative resistance as shown in Fig. 4.9. This means that for thin orifices and low frequencies, the resistance could be an alternative indication for the prediction of flow instability.

Fig. 4.11 shows the eigenvalues of the dissipation matrix as an index for the minimum and maximum acoustic dissipation/generation potentiality. These results identify the context for energy dissipation/generation for thin orifices as discussed in section 4.2.2. One of the eigenvalues is zero and the other determines whether the system is passive or active. The absorption coefficient values in Fig. 4.10 are about half of the non-zero eigenvalue as a result of Eq. (4.29), since the acoustic excitation shape $[\hat{p}_{ui}; \hat{p}_{dr}]$ is $[1; 0]$ for upstream excitation with an anechoic end at the downstream side, which is a combination of two basic mode shapes $\mathbf{Q}_1, \mathbf{Q}_2$ with coefficients $a_1 = \sqrt{2}/2, a_2 = \sqrt{2}/2$ in Eq. (4.29) and the energy absorption coefficient is a result of $|a_1|^2 \xi_1 + |a_2|^2 \xi_2$. It indicates that the non-zero eigenvalue is only an indicator for the maximum acoustic dissipation/generation potentiality. The real absorption coefficient should vary between the two eigenvalues, and depends on the incident waves from the upstream and downstream sides.

Chapter 5

Impedance eduction technique for acoustic liner with grazing flow

In this chapter, the experimental setup and techniques that have been used for the impedance identification are presented. First, the grazing flow test rig used in the current study is introduced. Different strategies and methods are further briefly reviewed. Comparisons have been made between the results from the German Aerospace Center (DLR) [53] and the results of a multi-mode matching method and a version of the straightforward method. The effects of shear flow and viscosity are studied numerically with a comparison of linearized Euler equations and linearized Navier-Stokes equations. Finally a systematic uncertainty analysis has been implemented using a multivariate analysis method.

5.1 Grazing flow facility for impedance eduction

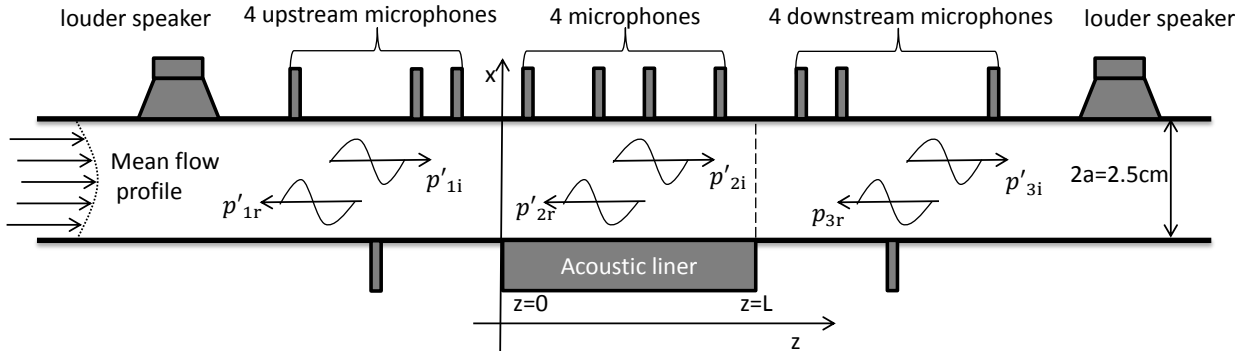


Figure 5.1: Sketch of liner test setup at KTH.

A sketch of the test setup is shown in Fig. 5.1. The acoustic liner sample is mounted in a rectangular test section, with liner width 70 mm and height 25 mm. The two acoustically hard side walls mean that the wave propagation can be simplified into a two-dimensional problem. The sound source on the upstream side produces an incident plane wave, p'_{1i} , which travels towards the lined section and is scattered at $z = 0$ into a reflected, p'_{1r} , and transmitted p'_{2i} wave. The waves propagating in the lined duct are further scattered at $z = L$ into reflected, p'_{2r} , and transmitted waves, p'_{3i} . The transmitted wave is further reflected giving p'_{3r} at the outlet side of the test rig. The numbering of the fields is as follows: 1 for the inlet hard duct,

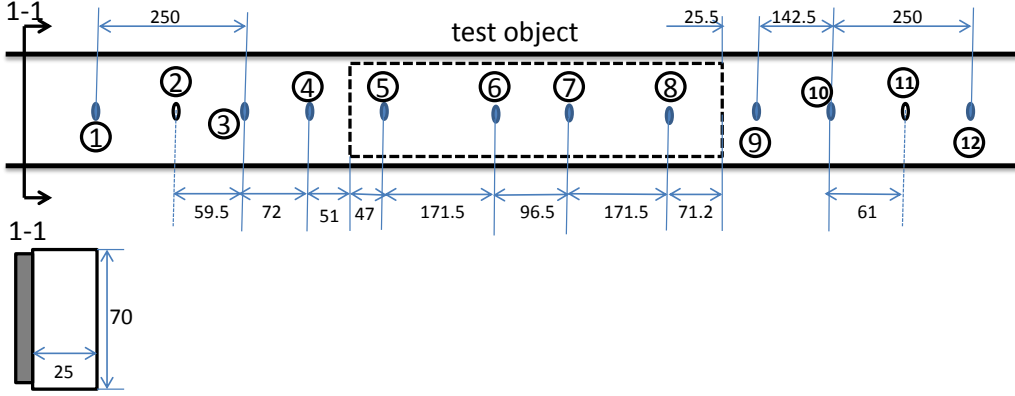


Figure 5.2: Sketch of liner test section with microphone (①-⑫) and Pitot tube position (⑤, ⑦), dimensions given in mm.

2 for the lined duct and 3 for the outlet hard duct. The wave propagation can be treated as two-dimensional for low frequency excitation because of the rigid boundary condition in the y direction. Fig.5.2 shows the geometry and transducer positions for microphones and Pitot tubes. At each end of the duct, acoustic sources and acoustic anechoic terminations are found, to be used for the acoustic scattering matrix identification using the two-source method [75]. The test object is a locally reacting single-degree-of-freedom Helmholtz resonator liner sample which was previously tested at DLR [53] and at NASA Langley [54]. The geometry of the DLR test tube is different from the KTH test rig with a width of 60 mm and a height of 80 mm. More details about the test setup can be found in [53]. Here the profiles in the KTH test rig are compared to the boundary layer theory for a fully developed turbulent channel flow [84, 85]

$$\frac{M}{M_\tau} = x^+, \text{ for } x^+ < 11 \text{ in the viscous sub-layer} \quad (5.1)$$

$$\frac{M}{M_\tau} = \frac{1}{0.41} \ln x^+ + 5.2, \text{ for } 1 - \left| \frac{x}{a} \right| \leq 0.1 \text{ in the logarithmic inner layer,} \quad (5.2)$$

$$\frac{M_{\max} - M}{M_\tau} = 6.3 \frac{x^2}{a^2}, \text{ for } 0 \leq \left| \frac{x}{a} \right| < 0.9 \text{ in the outer zone,} \quad (5.3)$$

where U_τ , U_{\max} are the friction velocity, the maximum velocity, which have to be determined

Case	U_{\max} (m/s)	U_0 (m/s)	U_τ (m/s)	$x_{\nu 1}$ (mm)	$x_{\nu 2}$ (mm)	$U_{\nu 2}$ (m/s)
I	34.88	31.07	1.54	0.11	0.49	22.70
II	68.80	60.31	2.85	0.058	0.26	42.01

Table 5.1: Bias and random error sources for different variables

from experimental results as shown in Tab. 5.1 using the bulk velocity U_0 . A local Reynolds number given by $x^+ = (a - |x|)U_\tau/\nu$ is used to determine the importance of viscosity and turbulence with air kinematic viscosity $\nu = 1.51 \times 10^{-5} \text{ m}^2/\text{s}$. The viscous sublayer thickness $x_{\nu 1}$ is the transition point for the region where a strong effect of molecular viscosity should be

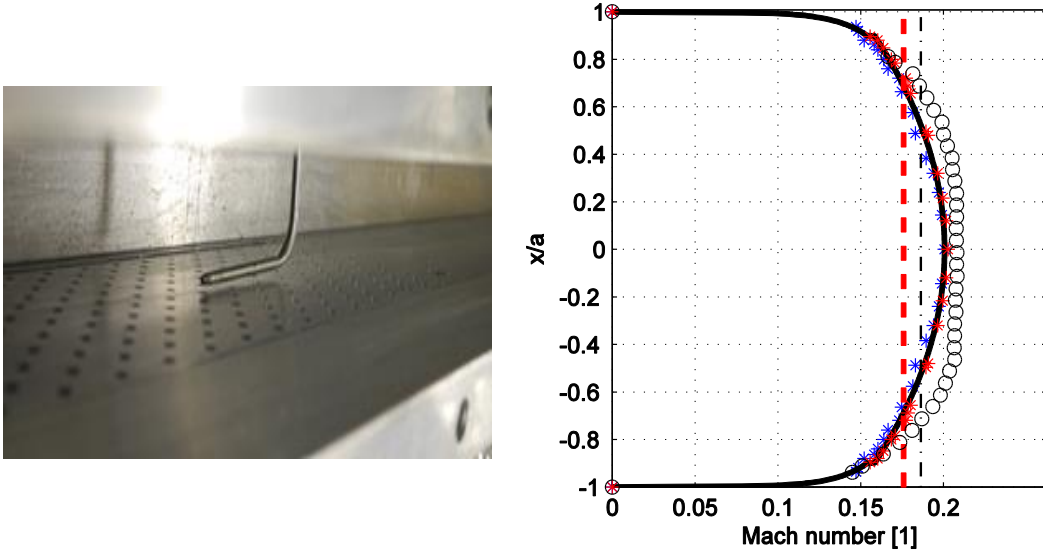


Figure 5.3: Mean flow profiles measurement with Pitot tube and the profile for the case of Mach number 0.2 measured at positions ⑤ (blue star markers), ⑦ (red star markers) according to Fig. 5.2, theoretical fully developed turbulent flow profile (solid line), and calculated mean Mach number (red dashed line); DLR mean flow profiles (black circles), DLR mean Mach number (black dot-dashed lines) [53].

taken into account with a local Reynolds number $x^+ = 11$. It will contribute significantly even far from the wall up to $x_{\nu 2}$ where $x^+ = 50$ with a local velocity $U_{\nu 2}$ calculated from Eq. (5.2). Two mean flow cases with different centreline Mach numbers ($M_{\max} \approx 0.1, 0.2$) have been tested and Tab. 5.1 shows their parameters. The good agreement between the experimental and theoretical fully developed flow profiles is shown in Fig. 5.3 for the case Mach number 0.2, which means that the flow in the duct can be considered as a fully developed turbulent flow. For convenience, the mean flow profiles and mean Mach number from the DLR test rig are plotted in the same figure. Only slight differences can be seen for the two test rigs, although the profile for the DLR results is flatter as a result of the wider tube ($a=40$ mm).

5.2 Strategy and methods

Mainly two different strategies can be implemented for impedance eduction: the closed loop minimization method [37, 38, 44, 48, 77] and the straightforward method [42, 47, 49]. The iterative method obtains impedance results using an iteration or minimization loop where experimental results are compared with simulated results starting from an initial impedance guess. The straightforward method firstly determines the axial wave numbers from measured pressure results, and impedance results are obtained from the wave number. A number of different methods have been implemented and discussed. The linearized Euler equations (LEE) method can handle plug flow as well as boundary layer shear flows. The linearized Navier-Stokes equations (LNSE) can include viscosity as well. The convected Helmholtz equation (CHE) is used with plug flow and employs the Ingard-Myers boundary condition and can be solved with a multi-mode matching method [44] with an assumption of pressure

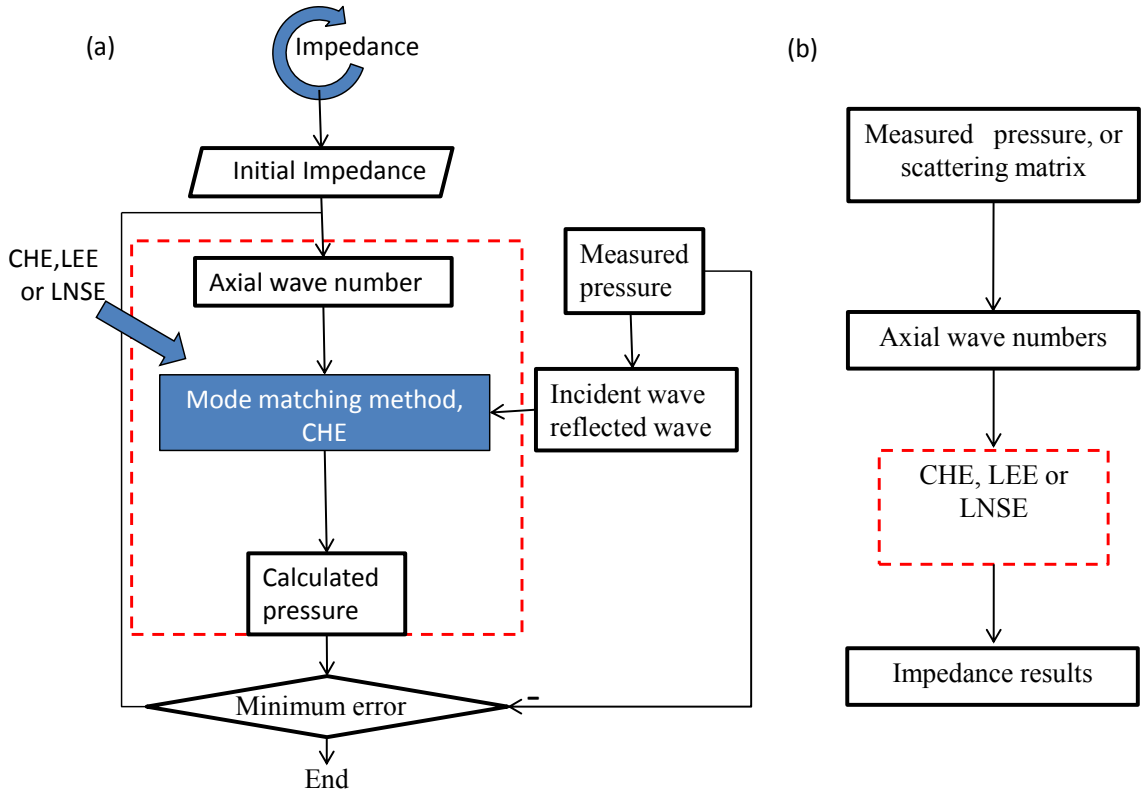


Figure 5.4: Strategies for impedance eduction based on different control equations: CHE-convected Helmholtz equation, LEE-linearized Euler equations, LNSE-linearized Navier-Stokes equations. (a): the iterative method, (b): the straightforward method.

and axial velocity continuity at interfaces between rigid section and lined sections($z = 0, L$),

$$\sum_{q=1}^N \hat{p}_1^{(q)}(x, 0) = \sum_{q=1}^N \hat{p}_2^{(q)}(x, 0), \quad (5.4)$$

$$\sum_{q=1}^N \hat{p}_1^{(q)}(x, L) = \sum_{q=1}^N \hat{p}_2^{(q)}(x, L), \quad (5.5)$$

$$\sum_{q=1}^N \left[\frac{\partial \hat{p}_{1i}^{(q)} / \partial z}{(k - M_0 k_{z1i}^{(q)})} + \frac{\partial \hat{p}_{1r}^{(q)} / \partial z}{(k + M_0 k_{z1r}^{(q)})} \right] \Big|_{z=0} = \sum_{q=1}^N \left[\frac{\partial \hat{p}_{2i}^{(q)} / \partial z}{(k - M_0 k_{z2i}^{(q)})} + \frac{\partial \hat{p}_{2r}^{(q)} / \partial z}{(k + M_0 k_{z2r}^{(q)})} \right] \Big|_{z=0}, \quad (5.6)$$

$$\sum_{q=1}^N \left[\frac{\partial \hat{p}_{2i}^{(q)} / \partial z}{(k - M_0 k_{z2i}^{(q)})} + \frac{\partial \hat{p}_{2r}^{(q)} / \partial z}{(k + M_0 k_{z2r}^{(q)})} \right] \Big|_{z=L} = \sum_{q=1}^N \left[\frac{\partial \hat{p}_{3i}^{(q)} / \partial z}{(k - M_0 k_{z3i}^{(q)})} + \frac{\partial \hat{p}_{3r}^{(q)} / \partial z}{(k + M_0 k_{z3r}^{(q)})} \right] \Big|_{z=L}, \quad (5.7)$$

where N is number of modes included and q is the mode number. Modal decomposition for rigid sections 1 and 3 has been given in section 2.2.1.2. Each mode in the lined duct can be represented by

$$\hat{p}_2^{(q)} = b_i^{(q)} \psi_i^{(q)} e^{-jk_{zi}^{(q)} \cdot z} + b_r^{(q)} \psi_r^{(q)} e^{-jk_{zr}^{(q)} \cdot (z-L)}, \quad (5.8)$$

where b_i , b_r are the complex amplitudes for incident and reflected waves, k_{zi} , k_{zr} are the corresponding axial wave numbers. ψ_i and ψ_r are the mode shapes of the incident and

reflected waves. The boundary conditions are $\partial p / \partial x|_{x=a} = 0$ at the rigid wall and the Ingard-Myers boundary condition (Eq. (2.26)) at the lined wall giving

$$\psi_{i,r} = e^{jk_{xi,r}x} + e^{jk_{xi,r}(2a-x)}. \quad (5.9)$$

The transversal wave numbers $k_{xi,r}$ can be expressed using the wave dispersion equation

$$k_x^2 = (k - M_0 k_z)^2 - k_z^2. \quad (5.10)$$

where subscripts i and r have been omitted for brevity.

5.2.1 Single-mode straightforward method

Theoretically, an infinite number of modes should be included in the mode matching method. Practically, a finite number of modes need to be used to approximately fulfill the boundary conditions. Here a simplified version using only one mode is presented for low frequency cases, which is based on the fact that the higher-order mode waves decay exponentially within the rigid sections and only the plane wave propagates. The interaction between modes in the lined section and plane in the rigid sections can be determined with a surface average of the mode shape (Eq. (5.9)) in the lined section given as

$$\Lambda^{(q)} = \frac{1}{2a} \int_{-a}^a \psi^{(q)} dx = \frac{1}{2jk_x^{(q)}a} [e^{3jk_x^{(q)}a} - e^{-jk_x^{(q)}a}]. \quad (5.11)$$

This index indicates that the amplitudes of the higher modes generated from incident plane wave are inversely proportional to the transverse wave numbers $k_x^{(q)}$ in the lined section. The value of the first transverse wave number is much smaller than the wave numbers of the higher order modes, which means that the first mode propagates most of the energy. If we only consider one mode, the plane wave component of pressure ($p(0), p(L)$) and axial acoustic velocity ($w(0), w(L)$) at the leading ($z = 0$) and trailing ($z = L$) cross-section simplify to

$$p(0) = b_i^{(1)} \Lambda_i^{(1)} + b_r^{(1)} \Lambda_r^{(1)} e^{-jk_{zr}^{(1)}L} + \varepsilon_1 p(0), \quad (5.12)$$

$$p(L) = b_i^{(1)} \Lambda_i^{(1)} e^{-jk_{zi}^{(1)}L} + b_r^{(1)} \Lambda_r^{(1)} + \varepsilon_2 p(L), \quad (5.13)$$

$$\rho c_0 w(0) = \frac{b_i^{(1)} \Lambda_i^{(1)} k_{zi}^{(1)}}{k - M_0 k_{zi}^{(1)}} - \frac{b_r^{(1)} \Lambda_r^{(1)} k_{zr}^{(1)} e^{-jk_{zr}^{(1)}L}}{k + M_0 k_{zr}^{(1)}} + \varepsilon_3 \rho c_0 w(0), \quad (5.14)$$

$$\rho c_0 w(L) = \frac{b_i^{(1)} \Lambda_i^{(1)} k_{zi}^{(1)} e^{-jk_{zi}^{(1)}L}}{k - M_0 k_{zi}^{(1)}} - \frac{b_r^{(1)} \Lambda_r^{(1)} k_{zr}^{(1)}}{k + M_0 k_{zr}^{(1)}} + \varepsilon_4 \rho c_0 w(L). \quad (5.15)$$

where $\varepsilon_1, \varepsilon_2, \varepsilon_3$ and ε_4 are the ratios of higher-mode contributions to the plane waves. In a single-mode approach, these ratios can be included as an error in the uncertainty analysis. For upstream excitation ($\hat{p}_{ui} = \hat{p}_{1i}^{(1)}$) with an anechoic downstream termination ($\hat{p}_{3r}^{(1)} = 0$), the scattering matrix (Eq.(3.4)) gives

$$p(0) = (1 + R_1) p_{1i}^{(1)}, p(L) = T_1 p_{1i}^{(1)}, \quad (5.16)$$

$$\rho c_0 w(0) = (1 - R_1) p_{1i}^{(1)}, \rho c_0 w(L) = T_1 p_{1i}^{(1)}, \quad (5.17)$$

Substituting these expressions as boundary conditions in Eqs. (5.12-5.15) and putting the contribution of higher-modes into the uncertainties in the wave reflections $R_{1,3}$ with a maximum error of $2\varepsilon(> \varepsilon(1 \pm R_1))$ and for the transition coefficients with an error of εT_1 gives

$$e^{-jk_{zi}^{(1)}L} = \frac{T_1}{1 - \eta_1}, \quad (5.18)$$

with

$$\eta_1 = \frac{R_1(k - (1 - M_0)k_{zr}^{(1)})}{(k + (1 + M_0)k_{zr}^{(1)})}, \quad (5.19)$$

For waves propagating towards the upstream side replacing T_1, R_1 and p_{1i} in Eqs.(5.16, 5.17) with T_3, R_3 and p_{3r} and substituting these equations in Eqs. (5.12-5.15) gives

$$e^{-jk_{zr}^{(1)}L} = \frac{T_3}{1 - \eta_3}, \quad (5.20)$$

with

$$\eta_3 = \frac{R_3(k - (1 + M_0)k_{zi}^{(1)})}{k + (1 - M_0)k_{zi}^{(1)}}, \quad (5.21)$$

Given scattering matrix $[R_1, T_3; T_1, R_3]$, the wavenumber for both downstream propagating waves and upstream propagating waves can be calculated, and the impedance can be obtained using the Ingard-Myers boundary condition (Eq.(2.26)) and the wave dispersion equation (Eq.(5.10)).

5.2.2 Numerical methods

The solution of linearized Navier-Stokes equations (Eqs.(2.27-2.30)) can be sought in the following modal forms:

$$\hat{p} = \sum_{q=1}^{\infty} \hat{p}^{(q)}(x) e^{-jk_z^{(q)}z}, \hat{u} = \sum_{q=1}^{\infty} \hat{u}^{(q)}(x) e^{-jk_z^{(q)}z}, \hat{w} = \sum_{q=1}^{\infty} \hat{w}^{(q)}(x) e^{-jk_z^{(q)}z}, \quad (5.22)$$

where $k_z^{(q)}$ are the axial wavenumbers, and $\hat{p}^{(q)}, \hat{u}^{(q)}, \hat{w}^{(q)}$ are the q th mode contributions for pressure and velocities at transversal and axial directions. The substitution of Eq. (5.22) into Eqs (2.27-2.30) leads to a one-dimensional problem

$$\frac{j(\omega - Uk_z^{(q)})\hat{p}^{(q)}}{\rho_0 c_0^2} - j\hat{k}_z^{(q)}\hat{w}^{(q)} + \frac{d\hat{u}^{(q)}}{dx} = 0, \quad (5.23)$$

$$\left[\frac{4}{3}\nu(k_z^{(q)})^2 + j(\omega - Uk_z^{(q)})\right]\hat{w}^{(q)} + \hat{u}^{(q)}\frac{dU}{dx} - \frac{j\hat{k}_z^{(q)}}{\rho_0}\hat{p}^{(q)} = \nu\left(\frac{d^2\hat{w}^{(q)}}{dx^2} - jk_z^{(q)}\frac{1}{3}\frac{d\hat{u}^{(q)}}{dx}\right), \quad (5.24)$$

$$[\nu(k_z^{(q)})^2 + j(\omega - Uk_z^{(q)})]\hat{u}^{(q)} + \frac{1}{\rho_0}\frac{d\hat{p}^{(q)}}{dx} = \nu\left(\frac{4}{3}\frac{d^2\hat{u}^{(q)}}{dx^2} - jk_z^{(q)}\frac{1}{3}\frac{d\hat{w}^{(q)}}{dx}\right), \quad (5.25)$$

The above equations further lead to the well-known Pridmore-Brown equation [86] for inviscid flow ($=0$),

$$\frac{d^2\hat{p}^{(q)}}{dx^2} + \frac{2k_z^{(q)}}{k - Mk_z^{(q)}}\frac{dM}{dx}\frac{d\hat{p}^{(q)}}{dx} + [(k - Mk_z^{(q)})^2 - (k_z^{(q)})^2]\hat{p}^{(q)} = 0 \quad (5.26)$$

with Mach number profile $M = U/c_0$. At the hard walls, boundary conditions are zero normal particle velocity

$$\hat{u}^{(q)}|_{x=a} = 0, \text{ or } \frac{d\hat{p}^{(q)}}{dx}|_{x=a} = 0. \quad (5.27)$$

At the liner surface, since the boundary layer profile is directly incorporated into the sound propagation model and the normalized impedance can be educed without introducing any further assumptions,

$$Z = -\frac{\hat{p}^{(q)}}{\rho_0 c_0 \hat{u}^{(q)}}|_{x=-a}, \text{ or } Z = \frac{jk\hat{p}^{(q)}}{d\hat{p}^{(q)}/dx}|_{x=-a}. \quad (5.28)$$

On the other hand, the Ingard-Myers boundary condition (Eq.(2.26)) is well accepted for plug flow cases ($M = M_0$)

$$Z = \frac{j(k - M_0 k_z^{(q)})^2 \hat{p}^{(q)}}{kd\hat{p}^{(q)}/dx}|_{x=-a}. \quad (5.29)$$

An additional non-slip boundary condition is also implemented for viscous flow

$$\hat{w}^{(q)}|_{x=\pm a} = 0. \quad (5.30)$$

The impedance can be identified from the Eqs. (5.23-5.25) based on a priori known complex wave numbers. Three methods were used, based on: the one-dimensional linearized Navier-Stokes equations, the Pridmore-Brown equation with shear flow and the Pridmore-Brown equation with uniform flow, which is identical to the convected Helmholtz equation labelled as LNSE, PBS and PBU.

5.2.3 The DLR's Method

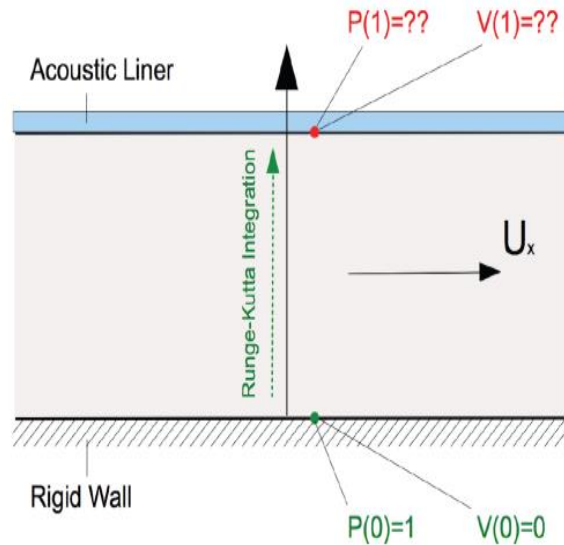


Figure 5.5: Schematic of the duct and the boundary conditions in the lined section fed into the Runge-Kutta integration [49].

In the method used by DLR, the axial wave number determination is simplified by only

using the transmission coefficients and assuming negligible effects from reflections $\eta_1, \eta_3 \ll 1$, which gives

$$k_{zI} = \frac{\ln|T|}{L}. \quad (5.31)$$

$$k_{zR} = \frac{-\arctan(\frac{T_I}{T_R})}{L}, \quad (5.32)$$

The calculated axial wave number was further put in a one-dimensional Pridmore-Brown equation including the effect of the profile of mean flow with non-slip wall boundary condition. A numerical Runge-Kutta integration method is used for impedance calculation by calculating $P(1)/V(1)$ in Fig. 5.5.

5.3 Impedance results and uncertainty estimation

5.3.1 Comparison of results from different test rigs

The advantage of the Convected Helmholtz equation mode matching method is the possibility for including higher-order modes. The contributions of higher-order modes (≥ 2) in the lined region is illustrated in Fig. 5.6, normalized by the first mode amplitude. The higher-order modes contribute less than 4% for all cases and can effectively be neglected, which demonstrated that a single-mode method is preferable for this case.

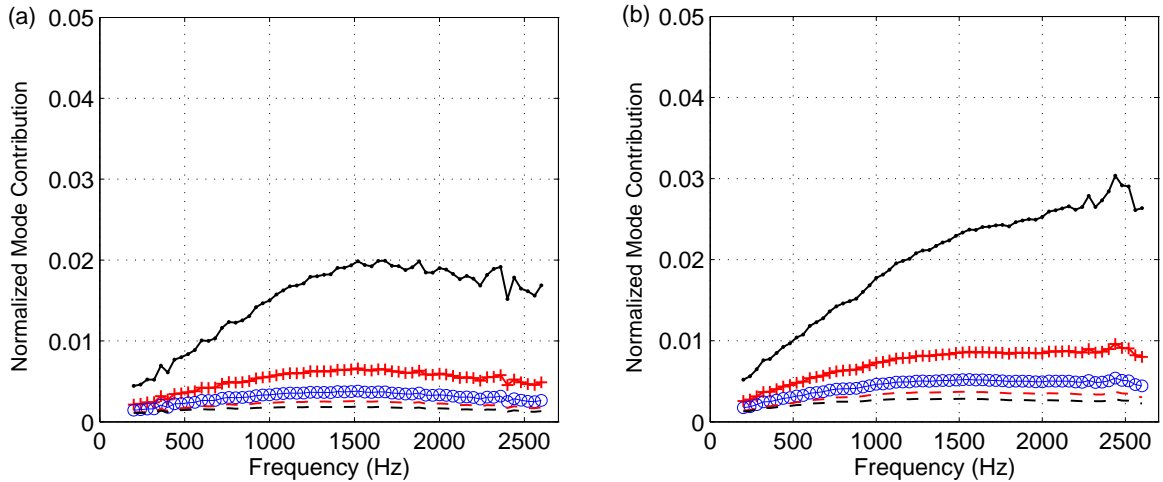


Figure 5.6: Normalized mode contribution $|b^{(q)}/b^{(1)}|$ ($N=6$ modes included, $q = 2, 3, \dots, 6$) for the propagating wave in the lined section for the flow case of Mach number 0.2. 2nd mode - black line with dots, 3rd mode - red line with plus signs, 4th mode - blue line with circles, 5th mode - red dashed line, 6th mode - black dashed line. (a) downstream propagating wave, (b) upstream propagating wave.

The liner impedance has been determined using the convected Helmholtz equation mode matching method [44] and the version of the straightforward single method described in section 5.2.1 using the Ingard-Myers uniform flow boundary condition, and the DLR method using a boundary condition with consideration of the shear flow. A comparison between the outcomes of these three impedance eduction methods for different flow speeds is presented in Fig. 5.7. Identical results in the whole frequency range have been obtained for the convected

Helmholtz equation mode matching method and the single-mode straightforward method, since higher-order modes have negligible contributions. It can be seen that the results are in good agreement in the whole frequency range compared to the DLR results. It means that similar impedance results could be obtained under the specific sound propagation situation (at least the same wave incident angle) plus the same mean flow situation even though the mean flow profile was different. This could imply that the mean flow profile has a small effect on impedance for inviscid flow at low frequencies.

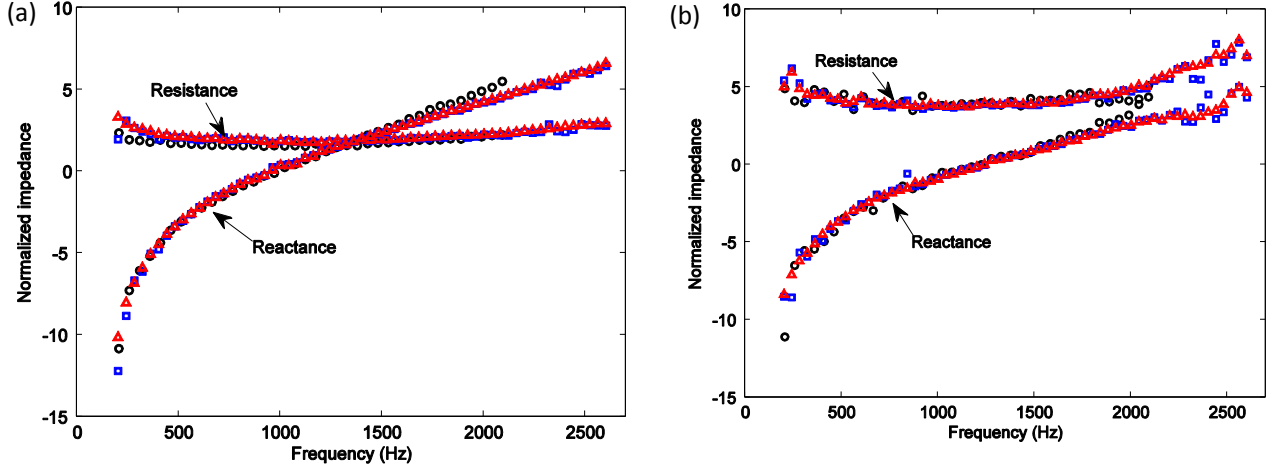


Figure 5.7: Comparison of educed normalized impedances for the upstream excitation case, blue squares convected Helmholtz equation, mode matching method, red triangles one-mode straight forward method according, black circles-DLR method, (a): Mach number 0.1, (b) Mach number 0.2. (Results of KTH have been normalized with a ratio of 70/60 for the difference of installed surface in different test rigs, 70 mm×25 mm in KTH test rig and 60 mm×80 mm in DLR test rig).

5.3.2 Numerical study with the linearized Navier-Stokes equations

5.3.2.1 Impedance results

Numerical simulations have been made to investigate the effect of shear flow and viscosity on impedance results with wavenumbers determined using transmission coefficients from Eqs.(5.31,5.32). A one-dimensional finite element method is employed for solving Eqs. (5.23-5.25) as well as the Pridmore-Brown equation Eq. (5.26) with shear flow and plug flow assumptions. The latter is equivalent to the one-dimensional convected Helmholtz equation. Fig. 5.8 shows the normal velocity and normal displacement ($\hat{u}/(\omega - k_z U)$) along a duct cross-section. For regions far from the liner wall, both normal velocity and normal displacement have almost identical results for the three cases. Compared with the uniform flow case, there is a difference in the normal velocity near the lined wall when including shear flow. By zooming in to the boundary layer, differences between LNSE and PBS results can be seen, illustrating the influence of viscosity within the boundary layer. The normal displacement results collapse except in the acoustic boundary layer region. Obviously, in the presence of viscosity, there is no continuity of normal velocity or displacement along the thin boundary layer. But for inviscid flow, the normal displacement continuity seems more reasonable than velocity continuity, which means that the Ingard-Myers boundary condition works for inviscid flow but not for viscous flow. However, even for the uniform flow case, the change of normal

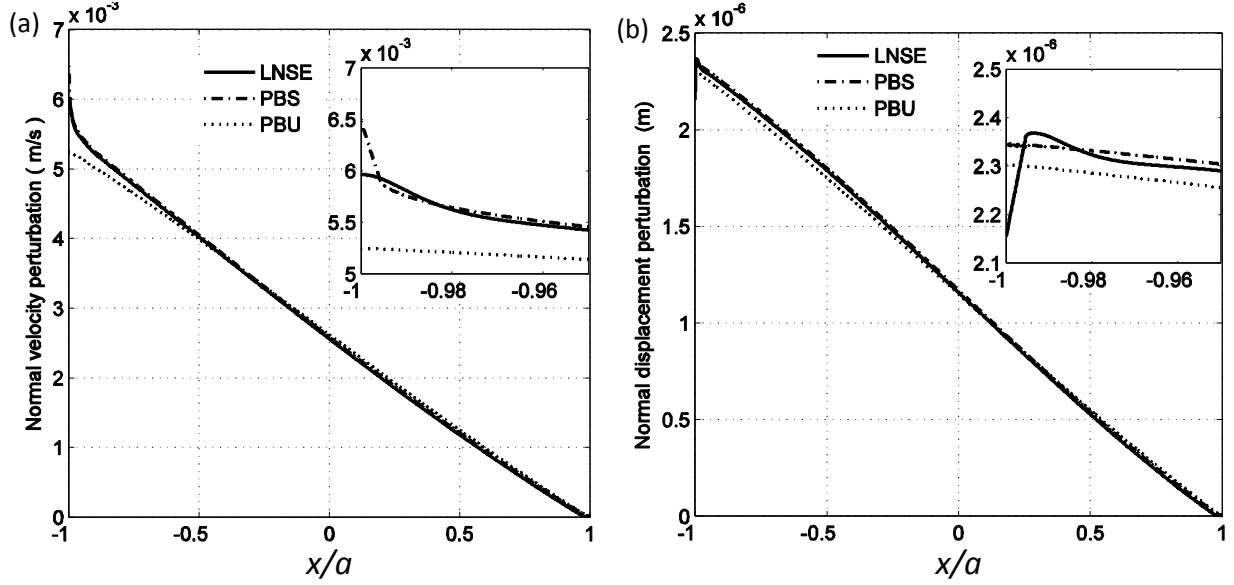


Figure 5.8: Normal velocity (a) and displacement (b) along a cross section of test tube for downstream propagating waves, 440Hz.

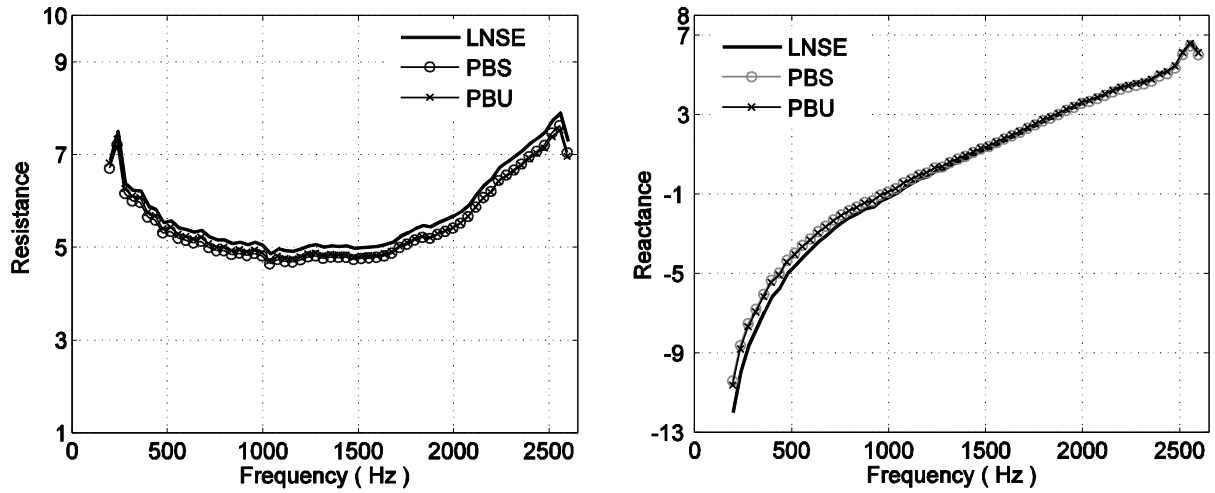


Figure 5.9: Educued impedance results for downstream propagation waves.

velocity and displacement is continuous along the boundary layer, which means theoretically there is no region or boundary layer that exhibits any constant velocity or displacement along the wall boundary layers. Theoretically, Eversman [87] shows that waves propagating within shear layers converge to the uniform flow case if the shear layer thickness goes to zero. And the convergence is independent of boundary layer shape, flow speed and driving frequency. Instead of displacement continuity along a thin boundary layer, the Ingard-Myers boundary condition could be considered as an equivalent relationship between the shear flow and uniform flow models. Geometries are the same for the two modes which give zero boundary layer thickness and shows good agreement of the normal displacement between the two models in Fig. 5.8 even within the wall boundary layer region.

The variation of normal velocity caused by the effect of viscosity within the lined wall boundary layer as shown in Fig. 5.8 will influence the impedance results. Fig. 5.9 shows the educued impedance results with and without viscosity effects included. There is some difference over the whole region for resistance results since the inclusion of viscosity extracts

some acoustic energy from the process of impedance identification. The reactance results exhibit more differences at low frequencies, which is in disagreement with the conclusion that viscosity can be ignored at low frequencies.

5.3.2.2 Two-dimensional wave propagation validation

A two-dimensional finite element method is employed to validate the impedance result with the software Comsol®. The computational region is shown in Fig. 5.10 with measured boundary conditions and nonslip boundary condition for linearized Navier-Stokes equations (LNSE, Eqs.(2.27-2.30) and linearized Euler equations (LEE, $\nu = 0$). The grids near the walls are refined to ensure that the first grid point at the lined wall is within the acoustic boundary layer $\sim \sqrt{2\nu/\omega}$. Since there are no noticeable differences for the impedance results

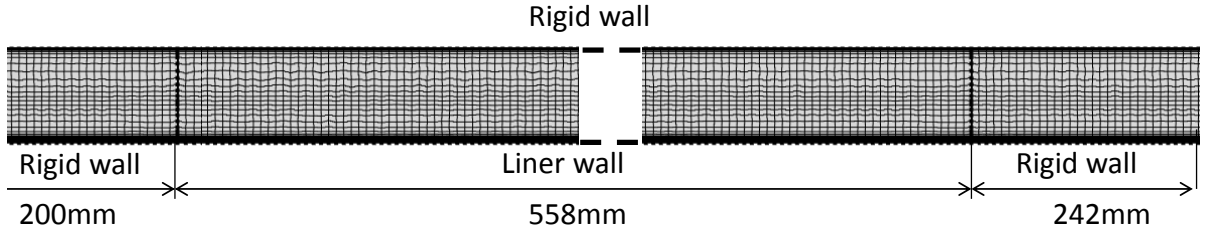


Figure 5.10: Computational domain showing the non-uniform finite element grid.

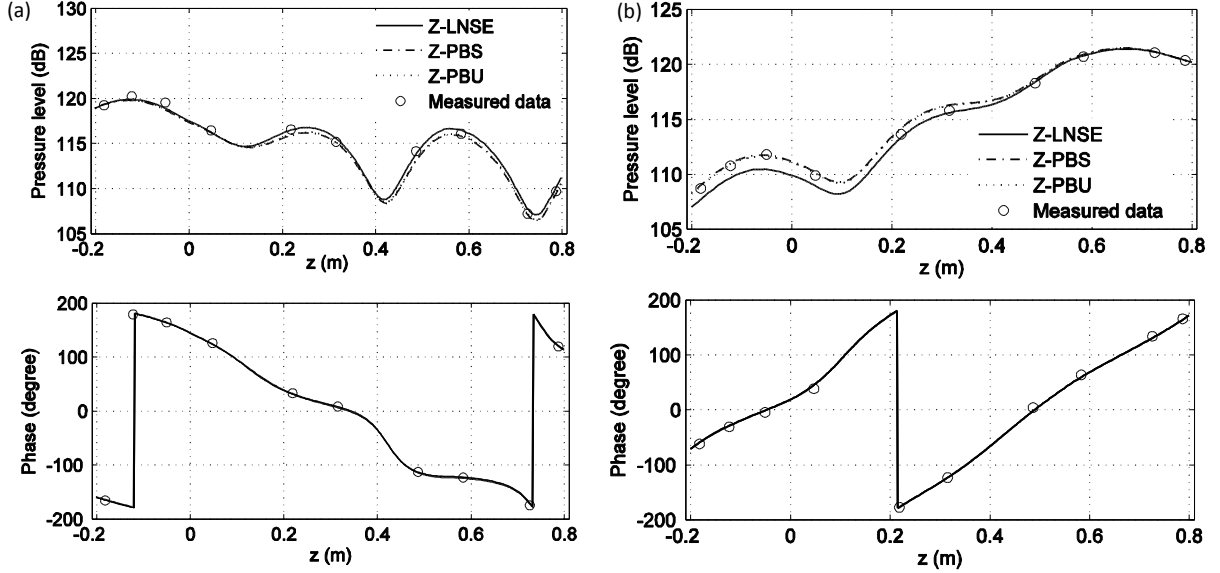


Figure 5.11: Pressure results with 2 dimensional LEE code coupled with different educed impedance results, 440Hz. (a): upstream excitation, (b): downstream excitation.

between the PBU and PBS as shown in Fig. 5.9, the pressure results are quite identical for the two cases as shown in Fig. 5.11 and Fig. 5.12. The agreement with experimental results is fairly good especially for the simulation results from the LEE code coupled with educed impedance from PBS, and from the LNSE code with educed impedance from the one-dimensional LNSE. This indicates that the impedance eduction technology should couple with the wave propagation code, which means that if the wave propagation code includes viscosity,

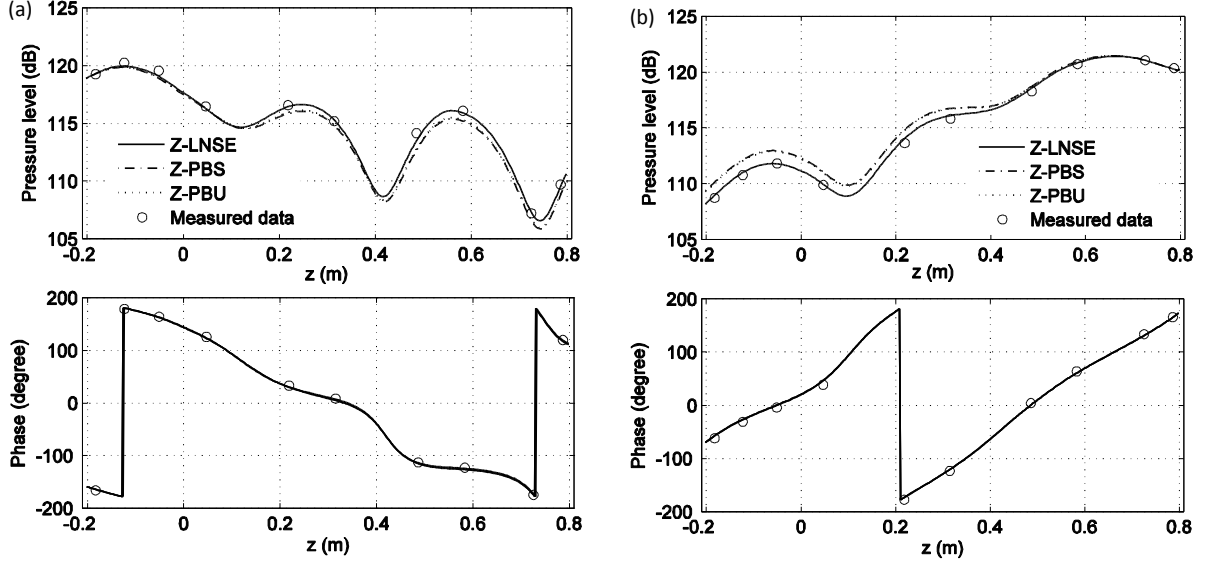


Figure 5.12: Pressure results with 2 dimensional LNSE code coupled with different educed impedance results, 440Hz. (a): upstream excitation, (b): downstream excitation

the process of impedance eduction should also consider viscosity. Noticeable differences are seen for the different impedance implementations with or without viscosity effects especially for the upstream propagating waves.

5.3.3 Uncertainty analysis based on the single-mode straightforward method

The influence of shear flow and viscosity has been discussed and results from different test rigs have been compared. There can be many different sources of uncertainties. These include errors from different measured quantities such as the flow speed, temperature, dimensions of liner length and the width of the test rig. The single-mode straightforward method is appropriate for uncertainty analysis because it is explicit and straightforward. Also, it can exclude numerical uncertainty which could appear in the multi-mode matching method, or any other numerical methods. The process only contains three steps:

1. Identify the axial wave number from transmission coefficients in Eqs. (5.31,5.32);
2. Determine the transverse wave number from wave dispersion equation in Eq.(5.10);
3. Calculate the impedance using Ingard-Myers boundary condition

$$Z = \frac{j(k - M_\delta k_z)^2 \hat{p}}{k} \frac{\hat{p}}{d\hat{p}/dx}|_{x=-a} = \frac{j(k - M_\delta k_z)^2}{k \cdot k_x \cdot \tan(2ak_z)}. \quad (5.33)$$

Many references assume that $M_\delta = M_0$. However, the local Mach number M_δ is different from the mean Mach number M_0 because of its local influence on liner impedance, while the mean Mach number should be used for the simulation of wave propagation. A summary of different error sources is given in Table 5.2 and the error propagation routine is shown in Fig. 5.13. Since the error in Mach number determination for the Ingard-Myers boundary condition

Variable	Error source	Error estimator
T	Higher-order modes contribution	Check with multi-mode matching method [44]
	Acoustic reflections at the leading and trailing liner boundaries	Check with scattering matrix results
	Random or bias errors from the two-microphone wave decomposition method	Estimate according to the suggestions in Ref. [88]
M_0	Calibration accuracy	Manufacturer's specifications
	Spatial averaging	Reduce by measuring more spatial points and estimate from the variance
	Random variation	Reduce by averaging and estimate from the variance
M_τ	Systematic error	Caused by incorrect assumption on Ingard-Myers boundary condition
L, a	Caliper accuracy	Manufacturer's specifications
	Random variation	Reduce by averaging and estimate from the variance

Table 5.2: Bias and random error sources for different variables

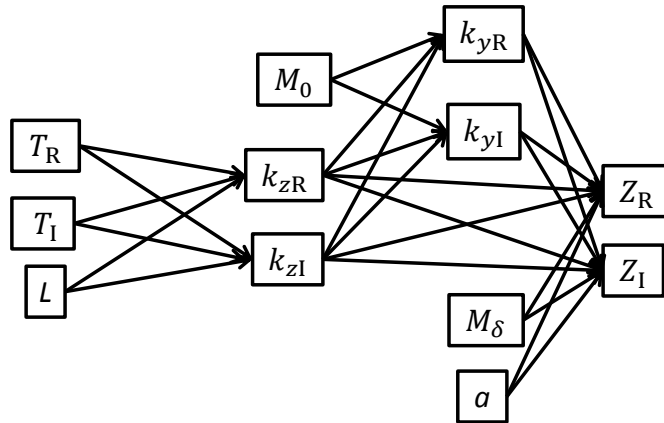


Figure 5.13: Uncertainty propagation routine for normalized impedance.

is systematic and could change the induced impedance results over the whole frequency domain, it is firstly assumed that $M_\delta = M_0$. Different levels of uncertainty have been studied for flow case of Mach number 0.2. Fig. 5.14 shows the uncertainty of impedance results with an absolute value of 3% and 5% error in the transmission coefficients, while Fig. 5.15 shows the uncertainty of impedance results from the change of mean Mach number. It is seen that the results at low frequencies are quite sensitive to the errors of transmission coefficients, while results are more sensitive to the uncertainty of Mach number at high frequencies. The educed impedance with uncertainty bars is presented in Fig. 5.16 for both downstream and upstream propagating waves with 3% relative uncertainty for transmission coefficients, 2% relative uncertainty for mean Mach number and 0.5 mm uncertainty for both the liner length and tube width. Considerable variations occur in resistance at high frequencies for downstream propagating waves, mainly caused by the uncertainty in the mean Mach number, while both downstream and upstream propagation results have large uncertainty at low frequency due to the uncertainty in determination of transmission coefficients.

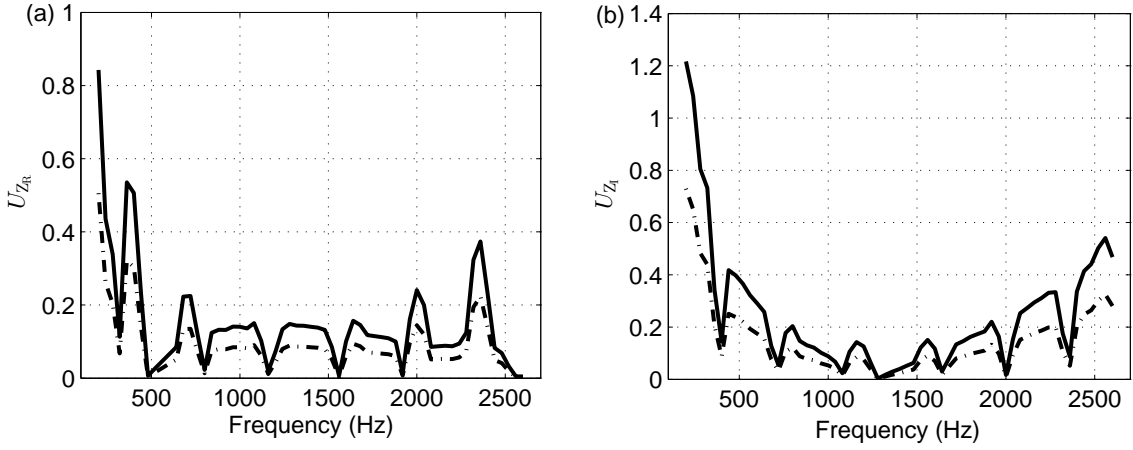


Figure 5.14: Expanded uncertainty of educed impedance for downstream propagating wave due to 3% (dash-dot line) and 5% (solid line) uncertainties in transmission coefficients. (a) uncertainty in resistance, (b) uncertainty in reactance.

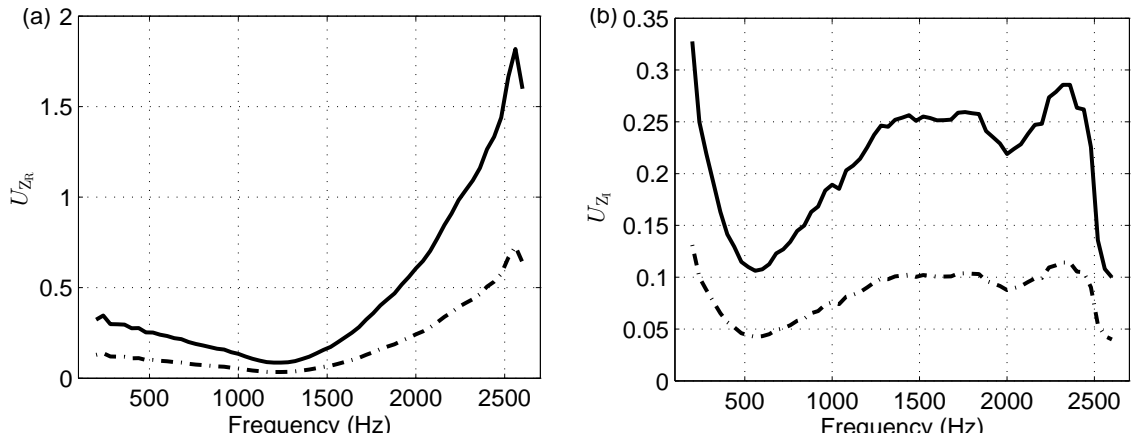


Figure 5.15: Expanded uncertainty of educed impedance for downstream propagating wave due to 2% (dash-dot line) and 5% (solid line) uncertainties in the mean Mach number. (a) uncertainty in resistance, (b) uncertainty in reactance.

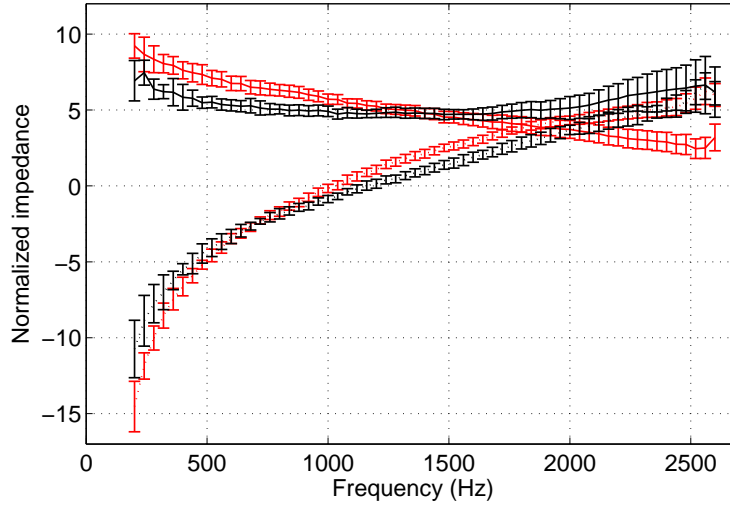


Figure 5.16: Identified impedance with uncertainty bars. Resistance - solid line, reactance - dash-dot line, downstream propagating wave - black line, upstream propagating wave - red line.

5.3.4 Discussion on Mach number used in the Ingard-Myers boundary condition

The original Ingard-Myers boundary condition is based on an ideally thin shear flow boundary layer. It means that the normal displacement on the lined wall is the same as that outside the thin boundary layer, where the Mach number is constant. Obviously, this ideal boundary layer never occurs in a real duct flow. The measured flow profile in Fig. 5.3 indicates that the point where the flow reaches the mean Mach number used in the Ingard-Myers assumption is about 4 mm. On the other hand, significant discrepancies in educed impedance results are observed in Fig. 5.15, comparing the results for excitation from two different directions, which was attributed to a failure of the Ingard-Myers boundary condition in Ref. [47]. A frequency-dependent parameter was introduced in order to collapse the educed impedance results for the two directions. However, another choice could be to reduce the boundary layer thickness by reducing the Mach number and moving the point closer to the lined wall. Theory for fully developed turbulent channel flow tells us that the closest point should be where $x^+ = 50$, which gives a boundary thickness about 0.26 mm in our case (Table. 5.1). This is the point where the viscosity starts to contribute significantly. On the other hand, different from the mean Mach number in the test tube, the local Mach number $M_\delta = 14.74U_\tau/c_0$ from Eq. (5.2) for $x^+ = 50$, is locally dependent on the friction velocity of the liner and independent of outer region flow in the test rigs. Applying this local Mach number based on friction velocity in the Ingard-Myers boundary condition (Eq. (5.33)), the impedance results could enable more reasonable experimental comparison for different test rigs and be easier for numerical implementation [89]. Fig. 5.17 shows educed impedance results both for our experimental results and the case of Ref. [47] implementing the proposed local Mach number assumption for the Ingard-Myers boundary condition in Eq. (5.33) and the mean Mach number for the wave dispersion equation in Eq. (5.10). Both cases show good agreement of the identified impedance for the two propagation directions, except at high frequencies in our test case. The reason for distortion at high frequencies could lie in the uncertainty in mean Mach number estimate for the wave propagation (dispersion equation). Recently, Jing [90] has shown that

the mean Mach number from a midspan profile results in a slight overestimation of the mean Mach number in the two-dimensional acoustic modelling and can affect the accuracy of the impedance results.

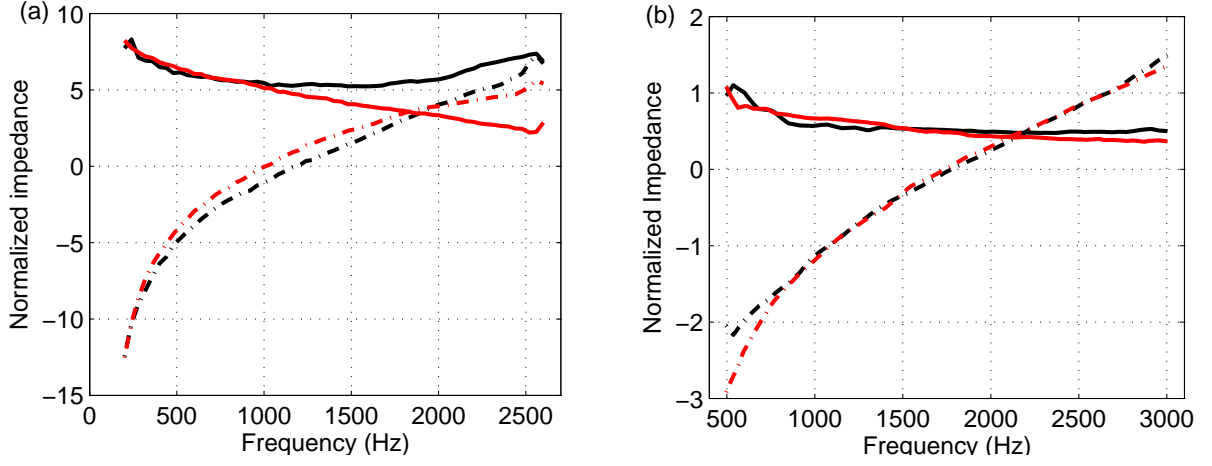


Figure 5.17: Educued impedance results with local Mach number, Resistance - solid line, reactance - dash-dot line, downstream propagating wave - black line, upstream propagating wave - red line. (a) Our experimental results, $M_\delta = 14.74M_\tau = 0.122$, (b) Renou and Auregan [47], $M_\delta = 14.74M_\tau = 0.137$.

Chapter 6

Concluding remarks and future work

6.1 Concluding remarks

Acoustic properties of an in-duct orifice with bias flow under high level acoustic excitations:

- Without bias flow, the acoustic impedance is only dependent on the inverse acoustic Strouhal number and there is a reasonably good agreement between analytical model results for the acoustic resistance. The reactance model based on Cummings effective length model captures the initial decrease with increasing excitation but has larger errors for high excitation levels;
- For the case with bias flow and low acoustic excitation levels, the resistance decreases with frequency, while the reactance increases;
- Orifice thickness influences the flow stability and the resistance tends to be negative while the reactance increases sharply with a relatively small increase in acoustic excitation level for a specific range of flow Strouhal numbers;
- For medium acoustic excitation levels, both resistance and reactance increase with acoustic excitation. A frequency-dependent minimum value exists for resistance when the acoustic flow velocity is of the same magnitude as, or slightly smaller than, the bias flow velocity;
- For sufficiently high acoustic excitation, the acoustic impedance is similar to that for the no bias flow case;
- Our new resistance model successfully captures the change of resistance from low to high acoustic excitation levels for low frequencies, but needs improvement for high frequencies;
- The nonlinear scattering matrix is useful for investigating the energy dissipation of the orifice, and the acoustic dissipation potentiality can be increased either by high-level acoustic excitation or by bias flow for low and medium acoustic excitation and frequencies far from the unstable region;
- Bias flow can in some cases cause flow instability and the experimental results show that high level acoustic excitation can influence the flow instability.

Impedance eduction techniques for grazing flow:

- Educated impedance results from different test rigs are in good agreement although slight differences exist, especially for high frequencies with higher flow speeds;
- Under low frequency excitation, higher-mode contributions are negligible and the straight-forward single method was shown to be efficient for the cases studied;
- Numerical results show that no velocity or displacement continuity exists in the vicinity of the lined wall;
- Our study indicates that the impedance eduction process should be consistent with that of the code of wave propagation computation, for example with the same assumption regarding viscosity;
- The errors in impedance results at low frequencies mainly depends on the variability of transmission coefficients, while the accuracy of mean Mach number is more important at high frequencies;
- The use of a local Mach number based on friction velocity improves the traditional use of the Ingard-Myers boundary condition and gives better agreement between the educated impedances for the two different wave propagation directions.

6.2 Future work

For future work, there are a few things in this PhD work that may be worth considering.

6.2.1 Impedance eduction technique under higher mode excitation

Until now, most experimental work has focused on plane wave excitation; there is no doubt that higher-mode waves exist in the aero engine application. Future works could develop current impedance eduction technique by including the effect of higher-order mode excitation. Practically full 3-D mean flow profile might be carefully considered. Ingard-Myers boundary condition could be further studied with different wave incident angles.

6.2.2 Permeability and flow instability for perforated liner

Usually, the perforated liner has been assumed to be impenetrable as a boundary condition. However, experimental results show that flow instability could occur at some flow speed. To the author's knowledge, no impedance model takes this effect into account. A new model could be built based on the impedance results without flow and considering the geometry of the perforated panel, such as porosity, orifice thickness, diameter, etc..

6.2.3 Numerical method development for the interaction of waves and turbulent flow

Bias flow can modify the impedance results and increase the damping of acoustic liners at low acoustic excitation levels. Grazing flow can increase the resistance while shifting the resonator frequency. In order to understand these phenomena, flow details around or near orifices should

be well understood. The mechanism of the interaction of waves and turbulent flow can be studied numerically. One idea could extend the one-dimensional harmonic matching method to two or three dimensions based on some numerical and analytical methods.

Chapter 7

Summary of Appended Papers

Paper A: Experimental investigation of an in-duct orifice with bias flow under medium and high level acoustic excitation

Lin Zhou, Hans Bodén

This paper experimentally investigates the acoustic properties of an orifice with bias flow under medium and high sound level excitation. A new experimental setup was carefully designed for a wide combination of different excitation levels and bias flow speeds. It covers the cases from when high level acoustic wave excitation causes flow reversal in the orifice to the cases where the bias flow maintains the flow direction. Orifices with two different edge configurations were tested for the influence of orifice thickness. Acoustic properties such as impedance, acoustic scattering matrix and energy absorption are investigated. The no flow experimental results have been compared with an analytical model based on Cummings' equation [18], while for high bias flow cases, the energy absorption was compared with theory from Howe [91]. Fairly good agreement has been obtained. Acoustic impedance results are extensively discussed under medium and high level acoustic excitation with different bias flow speed. A nonlinear scattering matrix is introduced and has proved to be useful for investigating the energy dissipation of the orifice and the acoustic dissipation potentiality which can be increased either by high level acoustic excitation or by the bias flow for low and medium acoustic excitation at frequencies far from the unstable region. Flow instability occurs for some bias flow cases and the high-level acoustic excitation can influence the instability.

Paper B: The effect of combined high-level acoustic excitation and bias flow on the acoustic properties of an in-duct orifice

Lin Zhou, Hans Bodén

In this paper, the so-called Cummings equation was modified to develop a theoretical model for impedance of an in-duct orifice. A novel orifice acoustic discharge coefficient model was developed both for cases with and without bias flow. A parameter based in the ratio of acoustic velocity and bias flow velocity was introduced for describing the transition from when high level acoustic dominates to when bias flow domains the acoustic properties. The harmonic balance method is used to obtain an analytical acoustic resistance model. There is fairly good agreement with the analytical model for resistance either for low or high acoustic excitation levels at low frequencies.

Paper C: Comparison of impedance eduction results using different methods and test rigs

Lin Zhou, Hans Bodén, Claus Lahiri, Friedrich Bake, Lars Enghardt, Stefan Busse-Gerstengarbe, Tamer Elnady

This paper studies impedance identification for acoustic liners with grazing flow. It contributes to a continuing effort to gain confidence in results obtained using different test rigs as well as different impedance eduction techniques. The latter includes the use of different equations for solving for the sound field in the lined section. The DLR reference liner sample HR-S2 studied is a locally reacting single-degree-of-freedom Helmholtz resonator liner which has previously been tested at DLR and NASA Langley. In this study, it is tested in a smaller scale facility at KTH, but under similar mean flow and sound pressure level conditions as in the previous studies. A good agreement has been obtained for different methods under the same plug flow assumption. The same trend but not identical effects of nonlinearity have been obtained with high levels of acoustic excitation. The effect of different flow Mach number assumptions is discussed in connection with the use of the Ingard-Myers boundary condition.

Paper D: Effect of viscosity on impedance eduction and validation

Lin Zhou, Hans Bodén

Traditionally, viscosity has been ignored due to the assumed negligible influence in the process of impedance eduction technology. However, this paper shows that viscosity has noticeable influence even at low frequencies. The investigation is based on a comparison study of the Linearized Euler equations and Linearized Navier-Stokes equations using a finite element simulation. In the process of impedance eduction, a one-dimensional straightforward method is proposed, which dramatically reduces the computational effort. Normal velocity and displacement have been obtained and discussed. Impedance results are further implemented into a two-dimensional wave propagation code. Finally simulation results have been compared and validated against experimental data. Our study, with similar conclusions to those in previous studies, indicates that the impedance eduction process should be consistent with that of the code for wave propagation computation, for example with the same assumption regarding shear flow and viscosity.

Paper E: A systematic uncertainty analysis for liner impedance eduction technology

Lin Zhou, Hans Bodén

A systematic framework based on multivariate analysis is presented in this paper to provide the 95% confidence interval uncertainty estimates in the process of impedance eduction. The impedance eduction method used is a single-mode straightforward method using transmission coefficients involving the classic Ingard-Myers boundary condition. The multivariate technique makes it possible to obtain an uncertainty analysis for the possibly correlated real and imaginary parts of the complex quantities. Different levels of component uncertainties have been studied for their contribution to the overall impedance results for both downstream and upstream propagating waves. The results show that at low frequencies the impedance results are highly sensitive to variation in transmission coefficient estimates, while they are more sensitive to the mean Mach number uncertainty at high frequencies especially for downstream propagating waves. The idea of using different Mach numbers for wave dispersion and in the Ingard-Myers boundary condition has been tested regarding the effect on impedance eduction. As a conclusion, a local Mach number based on friction velocity is introduced and validated using both our own experimental results and those from previous studies.

References

- [1] Lisa Goines, Louis Hagler, et al. Noise pollution: A modern plague. *Southern Medical Journal*, 100(3):287, 2007.
- [2] EEA, editor. *Noise in Europe 2014*. EEA (European Environment Agency), 2014.
- [3] Rolls-Royce plc, editor. *The jet engine*. Rolls-Royce plc, 1992.
- [4] Allan D Pierce et al. *Acoustics: an introduction to its physical principles and applications*. McGraw-Hill New York, 1981.
- [5] Dah-You Maa. Potential of microperforated panel absorber. *the Journal of the Acoustical Society of America*, 104(5):2861–2866, 1998.
- [6] LJ Sivian. Acoustic impedance of small orifices. *The Journal of the Acoustical Society of America*, 7(2):94–101, 1935.
- [7] J. W. S. Rayleigh. *The theory of sound*. London, Macmillan and co., 1877.
- [8] U Ingård and S Labate. Acoustic circulation effects and the nonlinear impedance of orifices. *The Journal of the Acoustical Society of America*, 22(2):211–218, 1950.
- [9] Uno Ingard. On the theory and design of acoustic resonators. *The Journal of the acoustical society of America*, 25(6):1037–1061, 1953.
- [10] Uno Ingard and Hartmut Ising. Acoustic nonlinearity of an orifice. *The Journal of the Acoustical Society of America*, 42(1):6–17, 1967.
- [11] MC Junger. Helmholtz resonators in load-bearing walls. *Noise Control Engineering*, 4(1):17–25, 1975.
- [12] Thomas Henry Melling. The acoustic impedance of perforates at medium and high sound pressure levels. *Journal of Sound and Vibration*, 29(1):1–65, 1973.
- [13] Ben T Zinn. A theoretical study of non-linear damping by helmholtz resonators. *Journal of Sound and Vibration*, 13(3):347–356, 1970.
- [14] Alan S Hersh and Thomas Rogers. *Fluid mechanical model of the acoustic impedance of small orifices*, volume 2682. US National Aeronautics and Space Administration, 1976.
- [15] AS Hersh, BE Walker, and JW Celano. Helmholtz resonator impedance model, part 1: Nonlinear behavior. *AIAA journal*, 41(5):795–808, 2003.

-
- [16] I-J Chang and A Cummings. A time domain solution for the attenuation, at high amplitudes, of perforated tube silencers and comparison with experiment. *Journal of sound and vibration*, 122(2):243–259, 1988.
 - [17] A Cummings. Acoustic nonlinearities and power losses at orifices. *AIAA journal*, 22(6):786–792, 1984.
 - [18] A Cummings. Transient and multiple frequency sound transmission through perforated plates at high amplitude. *The Journal of the Acoustical Society of America*, 79(4):942–951, 1986.
 - [19] Xiaodong Jing and Xiaofeng Sun. Numerical simulation on the nonlinear acoustic properties of an orifice. *AIAA Journal*, 38(9):1565–1572, 2000.
 - [20] Xiaodong Jing and Xiaofeng Sun. Discrete vortex simulation on the acoustic nonlinearity of an orifice. *AIAA journal*, 38(9):1565–1572, 2000.
 - [21] Xiaodong Jing and Xiaofeng Sun. Sound-excited flow and acoustic nonlinearity at an orifice. *Physics of Fluids (1994-present)*, 14(1):268–276, 2002.
 - [22] PD Dean and BJ Tester. Duct wall impedance control as an advanced concept for acoustic impression. 1975.
 - [23] MS Howe. On the theory of unsteady high reynolds number flow through a circular aperture. *Proceedings of the Royal Society of London. A. Mathematical and Physical Sciences*, 366(1725):205–223, 1979.
 - [24] Jeff D Eldredge and Ann P Dowling. The absorption of axial acoustic waves by a perforated liner with bias flow. *Journal of Fluid Mechanics*, 485:307–335, 2003.
 - [25] S Mendez, J Eldredge, F Nicoud, T Poinot, M Shoeybi, and G Iaccarino. Numerical investigation and preliminary modeling of a turbulent flow over a multi-perforated plate. In *Proceedings of the Summer Program*, page 1, 2006.
 - [26] T Luong, MS Howe, and RS McGowan. On the rayleigh conductivity of a bias-flow aperture. *Journal of Fluids and Structures*, 21(8):769–778, 2005.
 - [27] Jochen Rupp, Jon Carrotte, and Adrian Spencer. Interaction between the acoustic pressure fluctuations and the unsteady flow field through circular holes. *Journal of Engineering for Gas Turbines and Power*, 132(6):061501, 2010.
 - [28] Qi Zhang and Daniel J Bodony. Numerical investigation and modelling of acoustically excited flow through a circular orifice backed by a hexagonal cavity. *Journal of Fluid Mechanics*, 693:367–401, 2012.
 - [29] AS Hersch and Bruce Walker. Effect of grazing flow on the acoustic impedance of helmholtz resonators consisting of single and clustered orifices. 1979.
 - [30] Edward J Rice. Theoretical study of the acoustic impedance of orifices in the presence of a steady grazing flow. *The Journal of the Acoustical Society of America*, 59(S1):S32–S32, 1976.

-
- [31] BE Walker and AF Charwat. Correlation of the effects of grazing flow on the impedance of helmholtz resonators. *The Journal of the Acoustical Society of America*, 72(2):550–555, 1982.
 - [32] MS Howe, MI Scott, and SR Sipcic. The influence of tangential mean flow on the rayleigh conductivity of an aperture. In *Proceedings of the Royal Society of London A: Mathematical, Physical and Engineering Sciences*, volume 452, pages 2303–2317. The Royal Society, 1996.
 - [33] Keith S Peat, Jeong-Guon Ih, and Seong-Hyun Lee. The acoustic impedance of a circular orifice in grazing mean flow: Comparison with theory. *The Journal of the Acoustical Society of America*, 114(6):3076–3086, 2003.
 - [34] PD Dean. An in situ method of wall acoustic impedance measurement in flow ducts. *Journal of Sound and Vibration*, 34(1):97–IN6, 1974.
 - [35] S SARIN and J KOOL. An experimental study of the acoustic impedance of helmholtz resonator arrays under a turbulent boundary layer. 1981.
 - [36] A Cummings. The effects of grazing turbulent pipe-flow on the impedance of an orifice. *Acta Acustica United with Acustica*, 61(4):233–242, 1986.
 - [37] Willie R Watson. A new method for determining acoustic-liner admittance in a rectangular duct with grazing flow from experimental data. 1984.
 - [38] Willie R Watson. A method for determining acoustic-liner admittance in ducts with sheared flow in two-cross-sectional directions. 1985.
 - [39] Michael G Jones, Tony L Parrott, and Willie R Watson. Comparison of acoustic impedance eduction techniques for locally-reacting liners. *AIAA paper*, 3306:2003, 2003.
 - [40] Tamer Elnady and Hans Bodén. An inverse analytical method for extracting liner impedance from pressure measurements. In *Proceedings of the 10th AIAA/CEAS Aeroacoustics Conference, Manchester, UK, May*, pages 10–12, 2004.
 - [41] Willie R Watson and Michael G Jones. Comparison of a convected helmholtz and euler model for impedance eduction in flow. *AIAA Paper*, 2643:2006, 2006.
 - [42] Xiaodong Jing, Sen Peng, and Xiaofeng Sun. A straightforward method for wall impedance eduction in a flow duct. *The Journal of the Acoustical Society of America*, 124(1):227–234, 2008.
 - [43] WR Watsonf MG Jonesl and TL ParrottIt. Investigation of an anomaly observed in impedance eduction techniques. 2008.
 - [44] T Elnady, Hans Bodén, and B Elhadidi. Validation of an inverse semi-analytical technique to educe liner impedance. *AIAA journal*, 47(12):2836–2844, 2009.
 - [45] Michael G Jones, WR Watson, and DM Nark. Effects of flow profile on educed acoustic liner impedance. In *16th AIAA/CEAS Aeroacoustics Conference, Stockholm, Sweden*, 2010.

-
- [46] WR Watson and MG Jones. Validation of a new procedure for impedance eduction in flow. In *16th AIAA/CEAS Aeroacoustics Conference, Stockholm, Sweden*, 2010.
 - [47] Ygaäl Renou and Yves Aurégan. Failure of the ingard–myers boundary condition for a lined duct: An experimental investigation. *The Journal of the Acoustical Society of America*, 130(1):52–60, 2011.
 - [48] Stefan Busse-Gerstengarbe, Christophe Richter, Frank H Thiele, Claus Lahiri, Lars Enghardt, Ingo Roehle, Piergiorgio Ferrante, and Antonio Scofano. Impedance eduction based on microphone measurements of liners under grazing flow conditions. *AIAA journal*, 50(4):867–879, 2012.
 - [49] Lars Enghardt, A Fischer, A Schulz, and S Busse-Gerstengarbe. Determination of the impedance for lined ducts with grazing flow. In *Proceedings of the 18th AIAA/CEAS Aeroacoustics Conference, AIAA*, volume 2243, pages 04–06, 2012.
 - [50] Estelle Piot and J PRIMUS ET F SIMON. Liner impedance eduction technique based on velocity fields. In *Proceedings of the 18th AIAA/CEAS Aeroacoustics Conference*, number 2012-2198, 2012.
 - [51] WR Watson and MG Jones. Evaluation of wall boundary conditions for impedance eduction using a dual-source method. *AIAA Paper*, 2199, 2012.
 - [52] Willie R Watson and Michael G Jones. A comparative study of four impedance eduction methodologies using several test liners. AIAA, 2013.
 - [53] Stefan Busse-Gerstengarbe, Friedrich Bake, Lars Enghardt, and Michael G Jones. Comparative study of impedance eduction methods, part 1: Dlr tests and methodology. In *19th AIAA/CEAS Aeroacoustics Conference*, pages 2013–2124, 2013.
 - [54] Michael G Jones, Willie R Watson, Brian M Howerton, and Stefan Busse-Gerstengarbe. Comparative study of impedance eduction methods, part 2: Nasa tests and methodology. In *Proceedings of the 19th AIAA/CEAS Aeroacoustics Conference, AIAA Paper*, pages 2013–2125, 2013.
 - [55] Leandro D Santana, Wim De Roeck, and Wim Desmet. Indirect acoustic impedance eduction in presence of flow based on an analytical two-port formulation. *Mechanical Systems and Signal Processing*, 48(1):388–403, 2014.
 - [56] MK Myers. On the acoustic boundary condition in the presence of flow. *Journal of Sound and Vibration*, 71(3):429–434, 1980.
 - [57] E Dokumaci. A note on transmission of sound in a wide pipe with mean flow and viscothermal attenuation. *Journal of sound and vibration*, 208(4):653–655, 1997.
 - [58] MS Howe. The damping of sound by wall turbulent shear layers. *The Journal of the Acoustical Society of America*, 98(3):1723–1730, 1995.
 - [59] Chenyang Weng, Susann Boij, and Ardeshtir Hanifi. The attenuation of sound by turbulence in internal flows. *The Journal of the Acoustical Society of America*, 133(6):3764–3776, 2013.

-
- [60] Uno Ingard. Influence of fluid motion past a plane boundary on sound reflection, absorption, and transmission. *The Journal of the Acoustical Society of America*, 31(7):1035–1036, 1959.
- [61] Yves Aurégan, Rudolf Starobinski, and Vincent Pagneux. Influence of grazing flow and dissipation effects on the acoustic boundary conditions at a lined wall. *The Journal of the Acoustical Society of America*, 109(1):59–64, 2001.
- [62] Edward J Brambley. Viscous boundary layer effects on the myers impedance boundary condition. In *Proceedings of the 15th AIAA/CEAS Aeroacoustics Conference*, number 2009-3241, 2009.
- [63] Axel Kierkegaard, Susann Boij, and Gunilla Efraimsson. A frequency domain linearized navier–stokes equations approach to acoustic propagation in flow ducts with sharp edges. *The Journal of the Acoustical Society of America*, 127(2):710–719, 2010.
- [64] Acoustics – determination of sound absorption coefficient and impedance in impedance tubes – part 1: Method using standing wave ratio, 1996.
- [65] AF Seybert and DF Ross. Experimental determination of acoustic properties using a two-microphone random-excitation technique. *the Journal of the Acoustical Society of America*, 61(5):1362–1370, 1977.
- [66] JY Chung and DA Blaser. Transfer function method of measuring in-duct acoustic properties. i. theory. *The Journal of the Acoustical Society of America*, 68(3):907–913, 1980.
- [67] Acoustics – determination of sound absorption coefficient and impedance in impedance tubes – part 2: Transfer-function method, 1998.
- [68] Hans Bodén and Mats Åbom. Influence of errors on the two-microphone method for measuring acoustic properties in ducts. *The Journal of the Acoustical Society of America*, 79(2):541–549, 1986.
- [69] Mats Åbom and Hans Bodén. Error analysis of two-microphone measurements in ducts with flow. *The journal of the acoustical society of America*, 83(6):2429–2438, 1988.
- [70] Todd Schultz, Mark Sheplak, and Louis N Cattafesta. Uncertainty analysis of the two-microphone method. *Journal of sound and vibration*, 304(1):91–109, 2007.
- [71] Fridolin P Mechel, PA Mertens, and WM Schilz. Interaction between air flow and airborne sound in a duct. Technical report, DTIC Document, 1965.
- [72] Bert Phillips. Effects of high-wave amplitude and mean flow on a helmholtz resonator. 1968.
- [73] SL Sarin and ER Rademaker. *In-flight acoustic mode measurements in the turbofan engine inlet of Fokker 100 aircraft*. NLR, 1994.
- [74] POAL Davies. Practical flow duct acoustics. *Journal of Sound and Vibration*, 124(1):91–115, 1988.

-
- [75] Mats Åbom. Measurement of the scattering-matrix of acoustical two-ports. *Mechanical Systems and Signal Processing*, 5(2):89–104, 1991.
- [76] Mats Åbom. A note on the experimental determination of acoustical two-port matrices. *Journal of Sound and Vibration*, 155(1):185–188, 1992.
- [77] Tamer Elnady. Modelling and characterization of perforates in lined ducts and mufflers. 2004.
- [78] Irving Bardshar Crandall. *Theory of vibrating systems and sound*. D. Van Nostrand Company, 1926.
- [79] Andrew B Bauer. Impedance theory and measurements on porous acoustic liners. *Journal of Aircraft*, 14(8):720–728, 1977.
- [80] Xiaodong Jing and Xiaofeng Sun. Effect of plate thickness on impedance of perforated plates with bias flow. *AIAA journal*, 38(9):1573–1578, 2000.
- [81] Claus Lahiri. Acoustic performance of bias flow liners in gas turbine combustors.
- [82] A Cummings and Walter Eversman. High amplitude acoustic transmission through duct terminations: theory. *Journal of Sound and Vibration*, 91(4):503–518, 1983.
- [83] Ph Testud, Yves Aurégan, P Moussou, and Avraham Hirschberg. The whistling potentiality of an orifice in a confined flow using an energetic criterion. *Journal of Sound and Vibration*, 325(4):769–780, 2009.
- [84] H Schlichting. *Boundary layer theory*. McGraw-Hill New York, 1979.
- [85] Stephen B. Pope. *Turbulent flows*. Cambridge Univ Press, 2011.
- [86] DC Pridmore-Brown. Sound propagation in a fluid flowing through an attenuating duct. *The Journal of the Acoustical Society of America*, 30(7):670–670, 1958.
- [87] Walter Eversman and Roy J Beckemeyer. Transmission of sound in ducts with thin shear layersconvergence to the uniform flow case. *The Journal of the Acoustical Society of America*, 52(1B):216–220, 1972.
- [88] Todd Schultz, Mark Sheplak, and Louis N Cattafesta. Uncertainty analysis of the two-microphone method. *Journal of sound and vibration*, 304(1):91–109, 2007.
- [89] Walter Eversman. The boundary condition at an impedance wall in a non-uniform duct with potential mean flow. *Journal of Sound and Vibration*, 246(1):63–69, 2001.
- [90] Xiaodong Jing, Sen Peng, Lixun Wang, and Xiaofeng Sun. Investigation of straightforward impedance eduction in the presence of shear flow. *Journal of Sound and Vibration*, 335:89–104, 2015.
- [91] Michael S Howe. *Acoustics of fluid-structure interactions*. Cambridge university press, 1998.

Part II

Appended Papers

